Loading Rubidium Atoms Into a Hollow Core Fiber

by

Yiwen Chu

Submitted to the Department of Physics
in partial fulfillment of the requirements for the degree of

Bachelor of Science

at the

MASSACHUSETTS INSTITUTE OF TECHNOLOGY

June 2007

Author .....
Department of Physics
May 11, 2007

Certified by .....
Vladan Vuletić
Lester Wolfe Associate Professor of Physics
Thesis Supervisor, Department of Physics

Accepted by .....
Professor David E. Pritchard
Senior Thesis Coordinator, Department of Physics

Loading Rubidium Atoms Into a Hollow Core Fiber

by

Yiwen Chu

Submitted to the Department of Physics
on May 11, 2007, in partial fulfillment of the
requirements for the degree of
Bachelor of Science

Abstract

We demonstrate a procedure for cooling, trapping, and transferring rubidium atoms into a hollow core photonic band gap fiber. The atoms are first collected in a magneto-optical trap (MOT) and then cooled using polarization gradient cooling. Magnetic traps are then used to confine and transfer the atoms toward the face of the fiber. An optical dipole trap formed using laser light propagating through the fiber guide the atoms and confine them away from the fiber walls. We hope to use this system to achieve large optical depths with possible applications to quantum computing.

Thesis Supervisor: Vladan Vuletić
Title: Lester Wolfe Associate Professor of Physics

0.1 Acknowledgments

I have had great pleasure in working with the people involved in this experiment, and I am very glad to have this opportunity to acknowledge them.

The first person I would like to thank is Prof. Vladan Vuletić, who first introduced me to the world of quantum physics and then to field of atomic, molecular, and optical physics. He taught my first course in quantum mechanics, and I could not have hoped for a more engaging and enlightening teacher. His has provided invaluable guidance and insight for the projects that I have worked on, and I feel very fortunate to have had the opportunity to learn from him.

Another person I am very grateful to is Vlatko Balic. He really runs the show on a daily basis, but always takes the time to answer my questions and give clear, patient explanations. Vlatko has taught me both the nittyy-gritty of the electronics and the big physical picture of our the experiment. It's always a pleasure to talk to him, even when we're sitting on the floor of the lab discussing why several MOSFETs have gone up in smoke.

There are many other wonderful people involved in this project. Professor Mikhail Lukin at Harvard University is the other leader of this project, and I feel very fortunate to have the opportunity to work on an experiment led by such great physicists. Misho Bajcsy is a great person to work with, and I thank him for his patience and good humor. David Brown and Yat Shan Au are my companions in the lab, and I'm sure all three of us now have expertise in soldering in the dark.

I would also like to acknowledge all the members of the Vuletic group for being so helpful and enthusiastic, both when I first started working in their labs and when I only made occasional visits from upstairs (often for the purpose of borrowing their equipment). Much thanks to my friends, who have kept me going through the past four years. My deepest gratitude goes to my parents, one of whom was the first person to teach me physics, and the other still reminds me every day why I started learning it in the first place.

Contents

List of Figures

List of Tables

Chapter 1

Introduction

Strongly interacting light-atom systems have recently been an area of great interest and advancement due to its possible applications in quantum computing and quantum information processing. Such applications require the control and facilitation of non-linear interactions between atoms and very weak electromagnetic fields such as single photons. For example, it has been proposed that through non-linear interactions with an atomic system, one photon could cause π phase shifts in another photon [1]. Such a system can act as a CNOT gate, which represents the basic building block of a universal quantum computer. The phase shift that results from the above scheme is proportional to d_0, or to σ/A, where σ is the atomic cross section. Here, A is the area of the light beam that passes through the atomic medium. d_0 is the optical depth, which is a measure of the opacity of the medium. It is defined through ratio of light intensity after passing through the medium to the initial intensity, which is given by $I/I_0 = e^{-d_0}$. For an atomic medium, the optical depth is $d_0 = nL\sigma$, where n is the density of atoms, L is the length of the sample that the light passes through. From these relations, we can see that the stronger interaction and larger phase shifts are achieved through a system where the atoms and light have a long length over which to interact, while both are confined to a small area in the transverse directions. As suggested in [1], such a geometry can be obtained by introducing atoms into a hollow core photonic band gap fiber. This thesis describes an experimental realization of a tightly confined light-atom system by loading Rubidium atoms into a hollow core

fiber.

Many parts of this experiment involve standard and commonly used techniques for manipulating atoms and light, such as various trapping and cooling schemes using laser light and magnetic fields. However, there are many unique aspects of the apparatus and timing sequence that enable us to guide cold Rb atoms into the fiber and study the interesting physics that such a novel system demonstrates. This thesis will first discuss the background and theoretical aspects of the experiment, and then show the specifics of our implementation. Chapter 2 briefly examines the principles behind the hollow core photonic band gap fiber and gives an overview of the experiment. It also by looks at the challenges behind putting atoms into a fiber and therefore motivates the setup that will be described in the following chapters. Chapter 3 discusses the theoretical aspects of the various cooling and trapping techniques we use, while chapter 4 describes our experimental apparatus. The particular aspect of the experiment that I have been focusing on is the control of currents through the various magnetic coils used in the experiment. This is described in detail in Chapter 5. Chapter 6 shows our current progress in controlling and loading the atoms. Finally, Chapter 7 gives a summary along with a description of future studies that can be done using the system

Chapter 2

The Hollow Core Fiber and Experimental Overview

2.1 The Hollow Core Photonic Band gap Fiber

In an optical fiber, light is confined in a core surrounded by cladding material. Conventional optical fibers have a core with higher reflective index than the cladding, and the light is guided along the core by total internal reflection. In 1999, however, Cregan et al. demonstrated a photonic band gap fiber (PBGF) that can guide light in a hollow core surrounded by a triangular lattice of hollow rods made from silica [2]. Instead of total internal reflection, the mechanism behind these hollow core fibers is the photonic band gap of the fiber structure [3].

In general, a certain structure of dielectric materials allow only light with particular bands of frequencies $\omega(\vec{k})$ to propagate through, where $\vec{k}$ is the wave vector of the light. In the simplest case of a uniform dielectric material, we just have $\omega = ck/n$, where $n = \sqrt{\epsilon\mu}$ is the index of refraction for the material. If a periodicity is added, however, modes of light with different $\vec{k}$ become coupled according to Bloch's Theorem, and the frequencies of different modes are altered depending on how the electromagnetic fields of the mode are distributed in the structure. For example, one can start with solutions of Maxwell's equations in a uniform material with dielectric constant ϵ and add a periodicity in the material. Using perturbation theory, we can

find how the frequencies of the modes are affected by the change. If E is the unperturbed electric field with frequency ω, and $\Delta\epsilon$ is the change in the dielectric constant, we find an expression for the first order change in frequency that looks familiar from time-independent perturbation theory in quantum mechanics

$$\Delta\omega = -\frac{\omega}{2}\frac{\int \Delta\epsilon |E|^2}{\int \epsilon |E|^2}. \tag{2.1}$$

Here, the integrals are over unit cell of the periodicity. We see that that modes with electric field more concentrated in regions with higher dielectric constant ϵ are shifted down more in frequency.

If we now plot ω vs. $\vec{k}$ in a band diagram, we would see a collection of bands of various shapes that have been shifted from the linear dispersion relation we started with. For complex structures in 3-D, such as optical fibers, the fields and band diagrams must be calculated numerically. Looking at the diagram, we might find that there are certain ranges of ω in which there are no allowed modes for any value of $\vec{k}$. This is then called a photonic band gap. No light with a frequency that lies within the photonic band gap can propagate in the material. For the same reasons, if we now add a defect to the periodic structure such as a hollow air core in the lattice of silica rods, it can alter the frequencies of certain modes and pull them into the gap region. This "defect mode" is localized in the defect created by the hollow core and decays exponentially in the surrounding lattice. We can then couple light into the fiber from the outside if such a mode exists in the region $\omega > ck$ (called the light cone of air, since light propagating in air must fall in this region).

Of course, the structure of the fiber must be carefully engineered to give it confined single modes with the correct frequency for the intended applications. The fiber used in our experiment (Crystal Fibre, HC-800-02) has a core diameter of 6.8 μm, surrounded by a periodic cladding of hexagonal air holes in silica[1]. The core is formed by removing seven unit cells of the cladding. The band gap is centered around 840 nm. The Rb D_1 and D_2 lines are at 795 nm and 780 nm, respectively, which are

[1]Data sheet at: http://www.crystal-fibre.com/products/airguide.shtm

at the edge of the band gap. However, since we are only using a 1.3 inch long piece of fiber, attenuation is not really a concern. To make sure that the fiber guiding a single mode, we can optimize the coupling by observing the spatial pattern of the transmitted light.

2.2 Atoms in PBGF's

There has been several previous experiments in introducing rubidium atoms into the hollow core of a PBGF. The main challenge in these experiments is that Rb vapor tends to adhere to the silica glass walls of the fiber core [4]. Even if some atoms do not become permanently lost, interaction with the walls causes decoherence, and the state of the atoms are modified in some uncontrollable fashion. This makes them unsuitable for the purpose of implementing quantum devices. Recently, Ghosh et al. performed an EIT experiment with room temperature Rb atoms in a fiber [4]. There, the method was to coat the core of the fiber with a layer of $C_{18}H_{35}$, which decreases the dephasing rate due to Rb-silica interactions. In addition, light-induced atomic desorption was used to knock Rb off the walls, creating a peak atom number of 8×10^5 atoms. However, the time available for making useful measurements is limited by the time it takes for an atom to traverse the fiber core and get stuck again after the desorbing beam is turned off. This can be estimated by $d/\bar{v} \sim 10$ns, where d is the diameter of the fiber core, and $\bar{v}$ is the thermal velocity of the atoms. In our experiment, we use an optical dipole trap to guide rubidium atoms into the hollow core PBGF. The atoms are confined by the trap to the center of the core so that they cannot interact with the walls. Such traps are not deep enough to capture a significant number of atoms at room temperature, so the atoms will first be trapped and cooled using a magneto-optical trap (MOT) and polarization gradient cooling. Using cold atoms also decreases the effects of Doppler broadening and allows us to spectrally resolve individual states when performing measurements. We transport the atoms from the MOT to the fiber using magnetic trapping techniques. The atoms are trapped against gravity using the MOT coils, and confined in the horizontal direction

using four wires forming a funnel. Then a biasing field is applied in the vertical direction to shift the atoms down toward the fiber. At the input face of the fiber, atoms with low enough temperatures can be loaded into the optical dipole trap and guided into the fiber. Once the cold atoms are inside the fiber, they provide a rich system for performing a wide variety of studies.

Chapter 3

Cooling and Trapping

3.1 The Magneto-Optical Trap

Over the past century, atoms have been useful for testing new theories and make precision measurements because they present a relatively simple, closed system. However, experiments soon became limited by effects related to the temperature of the atoms, such as Doppler broadening. Therefore, many methods were tried to cool and confine atoms. In modern experiments, the most widely used method for creating cold samples of atomic vapor is the magneto-optical trap (MOT), which was first demonstrated in 1987 [5]. In a MOT, the atoms are cooled and trapped using the recoil force when photons are scattered off an atom [6, 7]. The momentum changed caused by this radiation-pressure force from each photon is very small ($\Delta v \approx 0.6$cm/s for ^{87}Rb). However, when a strong atomic transition is excited, the atom can scatter more than 10^7 photons per second, and a room temperature ^{87}Rb atom can be stopped in a few ms.

To cool the atoms, we make the scattering rate velocity dependent using the Doppler effect. An atom moving at a velocity v along the direction of the laser beam will see the laser frequency ν_{laser} shifted by $(-v/c)\nu_{laser}$. Therefore, if ν_{laser} is tuned beneath the transition frequency of the atomic resonance, more photons will be scattered when the atom is moving toward rather than away from the beam due to the upshift in frequency, as shown in Fig. 3-1. Using three pairs of counter-propagating

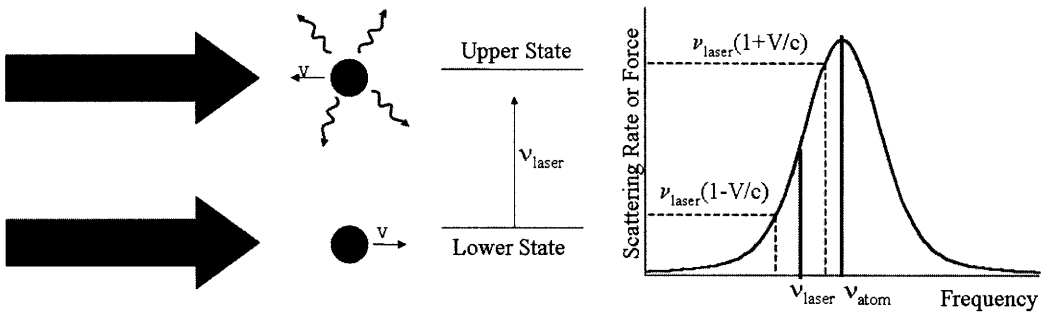

Figure 3-1: Scattering rate dependence on Doppler shift.
The laser frequency, which is tuned slightly below the atomic transition, is shifted due to the velocity of the atom. From the graph of scattering rate versus frequency, a bigger force is exerted on counter-propagating atoms.

beams, we can apply a force that opposes the motion of the atoms in the x, y, and z directions. If Δ is the detuning of the laser, γ is the decay rate of excited state, and s_0 is the on-resonance saturation parameter, the damping force from a pair of beams is given by [8]

$$\vec{F} = \frac{8\hbar k^2 \delta s_0 \vec{v}}{\gamma(1 + s_0 + (2\Delta/\gamma)^2)^2} \equiv -\beta\vec{v}. \tag{3.1}$$

in the limit of low laser intensity. This damping of the atomic motion cools the atoms and results in what is known as "optical molasses" [9].

Although the atoms are cooled using the laser beams, they must be confined to the region where the beams intersect. This can be done by using a magnetic field to produce Zeeman shifts in the energy levels of the atom. This idea is illustrated in Fig. 3-2 for a simple two-state system. Suppose that the atomic transition has a J=0 ground state and a J=1 excited state. In a magnetic field that varies linearly in z, the $m_J = -1$ states of atoms on the +z side are Zeeman shifted to lower energy, while the $m_J = +1$ states are shifted up in energy. The opposite happens for atoms on the -z side. Excited states with lower energy are closer to being on resonance with the laser. By applying a σ^+ laser beam that excites $|J = 0, m_J = 0\rangle \rightarrow |J = 1, m_J = +1\rangle$ transitions from the -z side, we can slow the motion of counter-propagating atoms to the left of the origin. Similarly, a σ^- laser beam from the +z that excites $|J =$

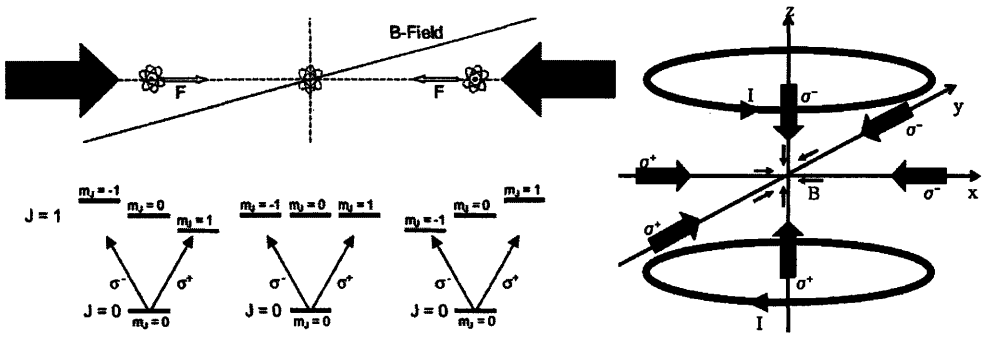

Figure 3-2: Cooling and trapping using position-dependent scattering. The J=1 excited state of an atom is Zeeman shifted using an inhomogeneous magnetic field. The lower energy m-states have transition frequencies closer to the laser frequency and are coupled to the J=0 ground state through σ^+ or σ^- polarized beams depending on their position. Cooling and trapping in three dimensions is achieved using a pair of anti-Helmholtz coils and three pairs of counter-propagating beams. Part of this drawing was taken from [7].

$0, m_J = 0\rangle \rightarrow |J = 1, m_J = -1\rangle$ transitions slows atoms to the right of the origin. Therefore, no matter where the atoms are, they will feel a force that pushes them back toward the origin. In fact, the motion of the atoms in the low laser intensity limit is that of a damped harmonic oscillator, with the force given by

$$\vec{F} = -\beta\vec{v} - \kappa\vec{r}, \tag{3.2}$$

where β is the damping coefficient defined in Eq. 3.1. The spring constant is given by

$$\kappa = \frac{\mu'\beta}{\hbar k}\frac{dB}{dz}. \tag{3.3}$$

Here, $\mu' \equiv \mu_B(g_e m_e - g_g m_g)$ is the effective magnetic moment of the transition from the ground (g) to the excited (e) state. g and m are the corresponding g-factors and magnetic quantum numbers of the two states, and μ_B is the Bohr magneton. The force leads to a damping rate of $\Gamma = \beta/M$ and an oscillation frequency of $\omega = \sqrt{\kappa/M}$. Then a characteristic time taken to restore atoms to the center of the trap is $2\Gamma/\omega^2$, which typically several ms.

Things are more complicated in three dimensions and with real atoms, which aren't simple two-state systems. Fig. 3-2 shows how an almost linear magnetic

field in all three directions can be achieved using a pair of anti-Helmholtz coils. It also shows the appropriately polarized laser beams. It turns out that, for a more complex set of atomic states, the MOT produces qualitatively similar results if the total angular momentum of the upper state is larger than that of the lower state [7, 5]. For trapping, we use the transition from the $5S_{1/2}(F = 2)$ to $5P_{3/2}(F' = 3)$ hyperfine states of the rubidium (see Fig. 4-2 in the next chapter for a diagram of hyperfine levels of ^{87}Rb. Though there are more intermediate Zeeman levels and the mechanism is more complex, the atoms will still be cooled and trapped due to a position dependent change in the transition frequency if the trapping beams are red-detuned from the transition frequency.

Due to Raman scattering involving the $5P_{3/2}(F' = 2)$ and $5P_{3/2}(F' = 1)$ levels, about 1 out of 1000 excitations will cause the atom to decay to the $5S_{1/2}(F = 1)$ state rather than back to the $5S_{1/2}(F = 2)$ state. This process of optical pumping takes the atom out of resonance with the trapping laser. Therefore, we need another "repump laser" to excite the atoms out of the F=1 state and allow them to decay back to the F=2 state, where they can be trapped again.

3.2 Polarization Gradient Cooling

The method of laser cooling described above is limited by the natural linewidth Γ of the the transition. The lowest velocity that can be achieved is given by $v = \sqrt{\hbar\Gamma/2m}$, at which point the Doppler width is much smaller than the natural linewidth [10]. This then corresponds to a temperature of $T_D = \hbar\Gamma/2k_B$, where T_D is called Doppler limit. For our cooling transition, $\Gamma/2\pi = 5.9$MHz and $T_D = 142\mu K$. To cool the atoms beyond this temperature, we use a technique called polarization gradient cooling, which is described in [11]. The lasers for the MOT are further detuned from resonance and provide a configuration of counter-propagating $\sigma^+ - \sigma^-$ beams. The atoms must be sufficiently cold so that they can be trapped by magnetic and dipole traps, which are the next stages in the loading process. In our case, polarization gradient cooling decreases the temperature by a factor of 3 below the Doppler limit.

3.3 Magnetic Traps

The MOT is gathered at the center of the magnetic fields provided by the MOT coils and the intersection of the laser beams, which is about 6mm above the top of the fiber. As the atoms are moved down toward the dipole trap at the face of the fiber, they must be confined in the horizontal direction to line them up with the fiber and prevent them from diffusing away. We also found that it was necessary to support the atoms in the vertical direction and lower them adiabatically, rather than just let them drop due to gravity. To do this, we use quadrupole magnetic traps, one of which is provided by the MOT coils, and the other by four thin wires that run along the fiber and through the MOT fields in a funnel-like shape. More detailed geometry and calculations follow in the next chapter. The general principle of is these traps is that an inhomogeneous magnetic field exerts a force on atoms with a magnetic dipole moment [12]. In a magnetic field, the energies of certain atomic states are shifted up by the Zeeman effect. Atoms in these states are called "low-field seekers" because their energies are minimized by a minimum in the magnitude of the magnetic field and can be trapped there. On the other hand, atoms in states whose energies are shifted down ("high-field seekers") would be trapped by a maximum in the field magnitude. Consider, for example, the ^{87}Rb $5S_{1/2}F = 2, m_F = 2$ state. The Zeeman shift in the weak field limit is given by

$$E_Z = \mu_B g_F m_F B, \tag{3.4}$$

where $\mu_B = e\hbar/2m_e$ is the Bohr magneton and the Landé g-factor in this case is $g_F = 1/2$ [13]. In the field provided by the MOT coils, atoms in this state are trapped in the vertical direction against gravity, while the quadrupole wires provide a potential well in the transverse directions. If an atom is in the $m_F = -2$ state, it will be forced out of the trap. So, before magnetic trapping, we must first optically pump the atoms into the $m_F = 2$ ground state. After the atoms are magnetically trapped, the zero of the field in the vertical direction can be shifted down to bring the atoms to the dipole trap at the face of the fiber.

3.4 Dipole Traps

The final mechanism for transporting atoms is the optical dipole trap, which guides the atoms into the fiber core and provides radial confinement that prevents the atoms from coming into contact with the fiber wall. Various types of optical dipole traps are described extensively in a review paper by Rudolf Grimm [14]. Classically, the optical dipole force arises from interaction of the laser light's electric field with an induced atomic dipole moment. The interaction potential turns out to correspond to the energy shift of the atomic ground state due to the AC Stark effect as calculated using second-order time-independent perturbation theory. For an alkali atom such as rubidium, the dipole potential due to linearly polarized light is given by

$$U(\vec{r}) = \frac{\pi c^2 \Gamma}{2\omega_0^3}\left(\frac{2}{\Delta_2} + \frac{1}{\Delta_1}\right) I(r). \tag{3.5}$$

Here, ω_0 is the transition frequency between the $5S$ and $5P$ states, and Δ_2, Δ_1 are the laser detunings from the $5S_{1/2} \rightarrow 5P_{3/2}$ and $5S_{1/2} \rightarrow 5P_{1/2}$ transitions, respectively. Finally, the spontaneous decay rate, which only depends on the electron orbital wavefunctions, is given by

$$\Gamma = \frac{\omega_0}{3\pi\epsilon_0\hbar c^3}\left|\langle l = 1|e\vec{r}|l = 0\rangle\right|^2. \tag{3.6}$$

From Eq. 3.5, we see that the potential seen by the atom is position dependent through the intensity profile of the laser. Our dipole trap has detunings $\Delta_2 < 0, \Delta_1 > 0$ and $|\Delta_2| < |\Delta_1|$, thus creating a negative potential well for a Gaussian laser beam.

Loading atoms into a hollow core fiber is not a simple maneuver, and requires us to use the variety of methods described above at different points in the process. Now that we've seen the principles behind these various cooling and trapping techniques, I will describe how they are implemented in our setup.

Chapter 4

Implementation of the Fiber Loading Apparatus

4.1 Lasers

All of the lasers we use must be frequency stabilized with the exception of the dipole trap laser. One set of lasers, used for trapping, cooling, and imaging, address the transitions between the hyperfine levels of the $5S_{1/2}$ and $5P_{3/2}$ fine structure states (the D_2 line). The second set of lasers used for probing atoms inside the fiber and performing EIT experiments have frequencies around the $5S_{1/2}$ to $5P_{1/2}$ (D_1) transitions. Each of the two sets are stabilized with respect to a reference laser, which is in turn locked to an atomic resonance.

4.1.1 Doppler-free DAVLL and Reference Laser Locking

To lock the reference lasers, we use a combination of saturated absorption spectroscopy and Dichroic Atomic Vapor Laser Lock (DAVLL), called Doppler-free DAVLL [15]. Doppler free spectroscopy was first developed to resolve features in atomic spectra that are obscured by Doppler broadening. This is done by directing two counter-propagating beams split from a single laser at the same collection of atoms[16]. One beam is the more intense pump beam, which excites atoms of velocity v along the

direction of the beam when it is at a frequency $\nu = \nu_0(1 + v/c)$, where ν_0 is the transition frequency of the atom. The other beam, which is called the probe beam, excites atoms with velocity $-v$ since it is propagating in the opposite direction. As the frequencies of the two beams are ramped simultaneously, they will only affect the same group of atoms when $\nu = \nu_0$ and $v = 0$. When this is the case, the pump beam will have already excited a large number of atoms, leaving fewer for absorption of the probe beam. We will then see a saturated absorption profile with a sharp Lorentzian dip (called the Lamb dip) in the center of the broad Doppler peak.

A unique feature of Doppler-free spectroscopy is crossover transitions. These transitions happen when atoms with nonzero Doppler shift $\delta\nu$ are excited by the pump beam with one transition at frequency ν_1, but are also the right velocity for the probe beam to be absorbed by a different transition ν_2. These relationships can be expressed as

$$\nu_1 = \nu_{co} + \delta\nu,\ \nu_2 = \nu_{co} - \delta\nu \Rightarrow \nu_{co} = (\nu_2 + \nu_1)/2 \tag{4.1}$$

Therefore, we expect to see these transitions at frequencies halfway between all pairs of hyperfine transitions. Of course, the same effect happens to atoms moving at the same velocity in the opposite direction if we just switch ν_1 and ν_2. So the crossover spectral lines will be twice the intensity of absorption caused by a single group of atoms at particular velocity, which will typically make them more intense than regular transitions observed for only zero velocity atoms. Compared to the Doppler broadened spectrum used in regular DAVLL locks, the Doppler-free spectrum has narrower and more intense lines that can be used for locking with higher frequency accuracy.

To lock lasers to a particular crossover transition, we split the reference laser into pump and probe beams, and send them through a Rb vapor cell enclosed in a solenoid. The vapor cell contains both isotopes of Rb, but we use the signal from ^{85}Rb for reference laser lock. The magnetic field generated by the solenoid Zeeman-shifts the energy levels of the atoms. If the probe beam is linearly polarized, the σ^+ and σ^- components will generate saturated absorption profiles that are shifted in frequency

by the same amount in opposite directions. Subtracting the two signals, we will get Doppler-free DAVLL signal that crosses zero at the transition frequency (see Fig. 4-1). The laser frequency can then be stabilized to the transition frequency by sending

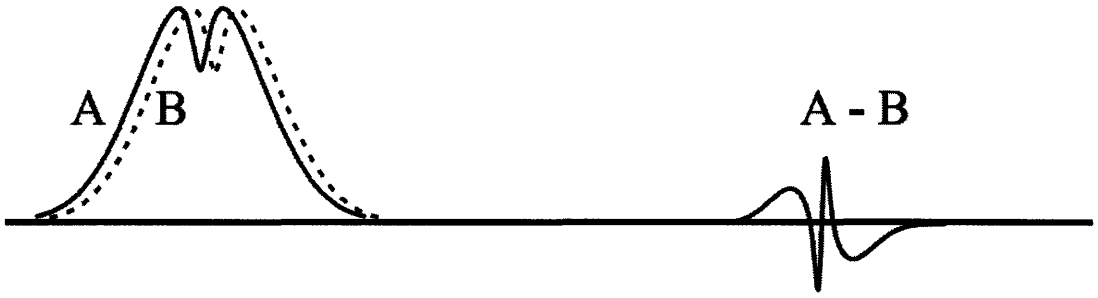

Figure 4-1: Illustration of Doppler-free DAVLL locking.
Two Zeeman shifted saturated absorption lines are subtracted to give an error signal (taken from [15]).

the signal through a proportional-integral (PI) feedback controller that corrects the frequency error by adjusting the current and cavity length of the reference lasers. In our setup, the D_2 reference laser is locked to the crossover transition between the $5S_{1/2}(F = 3) \rightarrow 5P_{3/2}(F' = 3)$ and $5S_{1/2}(F = 3) \rightarrow 5P_{3/2}(F' = 4)$ lines of ^{85}Rb, while the D_1 reference laser is locked to the crossover transition between the $5S_{1/2}(F = 3) \rightarrow 5P_{1/2}(F' = 2)$ and $5S_{1/2}(F = 3) \rightarrow 5P_{1/2}(F' = 3)$ lines of ^{85}Rb.

4.1.2 Lasers for Trapping, Cooling, etc.

As described in the previous chapter, trapping and cooling atoms using a MOT requires a trapping laser and a repumping laser. The repumping laser is locked to the $5S_{1/2}(F = 1) \rightarrow 5P_{3/2}(F' = 2)$ transitions of ^{87}Rb. The trapping laser is red detuned from the $5S_{1/2}(F = 2) \rightarrow 5P_{3/2}(F' = 3)$ transition of ^{87}Rb by 20 MHz for MOT collection and 140 MHz for polarization gradient cooling. In addition, we use another laser locked to the $F = 2 \rightarrow F' = 3$ line to do absorption imagining on the atoms outside of the fiber. This imaging laser can also be used to probe the atoms inside the fiber. These three lasers are frequency stabilized by locking to the D_2 reference laser as described in the next section. Currently, only the probe laser, which is on the $5S_{1/2}(F = 2) \rightarrow 5P_{1/2}(F' = 2)$ transition, is locked to the D_1 reference laser.

The dipole trap laser is a free-running diode laser with wavelength ~785nm, since fluctuations in the frequency will only slightly change the depth of the trap. In the future, we will add a second laser on the D_1 $F = 1 \rightarrow F' = 2$ transition to perform EIT measurements. Fig. 4-2 shows the various laser frequencies and energy level diagrams for ^{87}Rb and ^{85}Rb. The list below gives characteristics of the various lasers

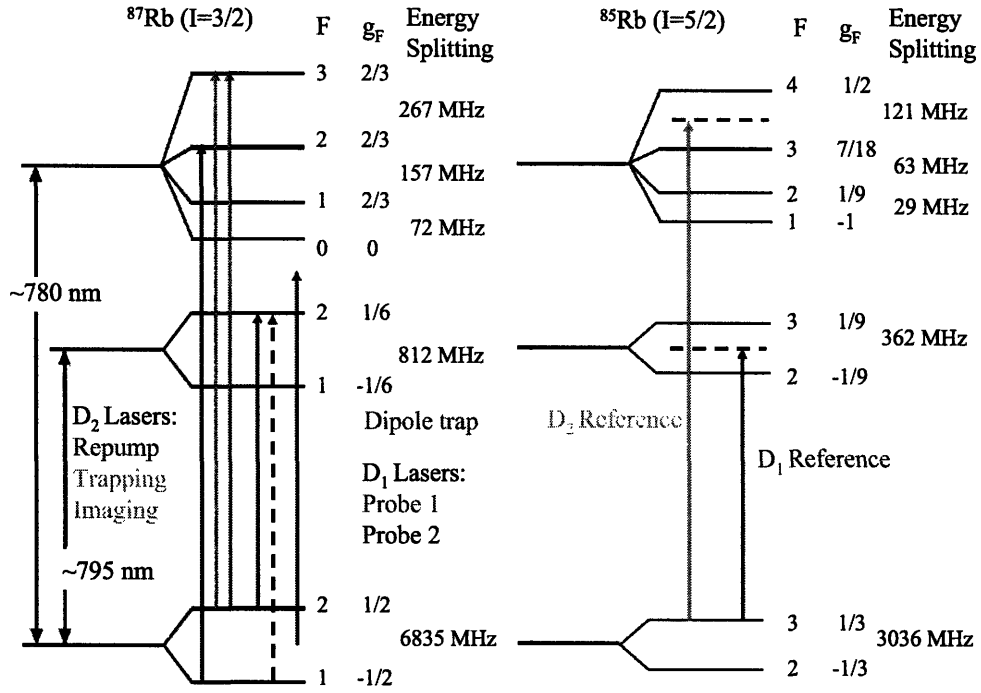

Figure 4-2: Partial energy level diagram of rubidium showing laser transitions. D_2 and D_1 lasers are locked to their respective reference lasers. Trapping laser is detuned 20 MHz for MOT collection, and 140 MHz for polarization gradient cooling. Dipole trap laser is free-running at ~785nm. Second probe laser is not in current setup.

used:

1. D_2 Reference laser

   - Sacher Lasertechnik TEC 50 series DFB laser.

- Locked to D_2 $F = 3 \rightarrow F' = 4$ and $F = 3 \rightarrow F' = 3$ crossover transition using Doppler-free DAVLL.
- Power Used: 20 mW at output. Split for locking three D_2 slave lasers.

2. Trapping Laser

   - Sacher Lasertechnik TEC-300 series tapered amplifier laser in Littrow configuration.
   - Locked to D_2 $F = 2 \rightarrow F' = 3$ transition
   - Frequency offset from D_2 reference laser: -1066 MHz plus detuning
   - Power used: 400 mW at output. 70-80mW into experiment after losses from fiber coupling, AOM, etc.
   - AOM: Isomet 1205C-2

3. Repump Laser

   - Sacher Lasertechnik TEC 50 series DFB laser.
   - Locked to D_2 $F = 2 \rightarrow F' = 3$ transition
   - Frequency offset from D_2 reference laser: 5.5 GHz
   - Power used: 30 mW at output. 10 mW into experiment after losses.
   - AOM: Isomet 1205C-2

4. Imaging/D_2 Probe Laser

   - ECDL-XXXXR extended cavity diode laser.
   - Locked to D_2 $F = 2 \rightarrow F' = 3$ transition
   - Frequency offset from D_2 reference laser: 5.5 MHz
   - AOM: Isomet 1205C-2

5. D_1 Reference Laser

   - ECDL-XXXXR external cavity diode laser.

- Locked to D_1 $F = 3 \rightarrow F' = 3$ and $F = 3 \rightarrow F' = 2$ crossover transition using Doppler-free DAVLL.
- Power Used: 15 mW at output.

6. D_1 Probe laser
   - Toptica DL 100 series external cavity diode laser.
   - Locked to D_1 $F = 2 \rightarrow F' = 2$ transition
   - Frequency offset from D_1 reference laser: -885.6 MHz
   - AOM: Crystal Tech 3080-122
7. Dipole Trap Laser
   - External cavity diode laser using Sharp GH0781JA2C laser diode
   - Free-running ~785 nm
   - Power Used: 90 mW at output, 25 mW into experiment.

4.1.3 Laser Locking

I will give a general overview of the laser lock system, while details on the electronics can be found in [17]. A diagram of the laser locking mechanism used is given in Fig. 4-3. Beams split from the reference laser and slave laser are combined through a beam splitter into a fast photodetector (Hamamatsu G4176-03). The photodetector acts as a mixer and produces a beat signal that has a frequency $\omega_{beat} = |\omega_{ref} - \omega_{slave}|$. This signal is then amplified by 40 dB and then compared to a reference frequency through a phase frequency detector (Analog Devices F4007). The reference frequency is provided by a direct digital synthesizer (Analog Devices 9959), which can output frequencies up to 160 MHz. Since the beat frequencies are in the range of a few gigahertz, it must be divided down before comparison to the reference frequency. This is done internally by the AD R4007, and the divider value can be set to a factor of N=8, 16, 32, or 64. After taking into consideration the frequency shift due to the acousto-optic modulator (AOM) used to control the slave lasers ($\pm 80 MHz$

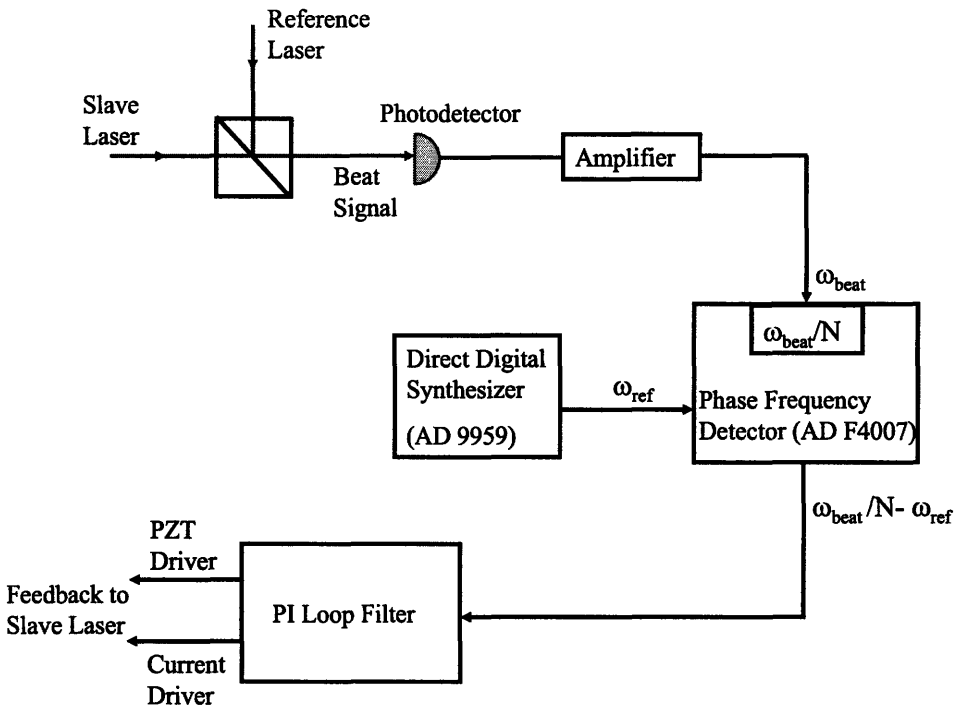

Figure 4-3: Diagram of system for locking a slave laser to the reference laser.

depending on the alignment), we can set the reference frequency appropriately to $\omega_{ref} = (\Delta\omega \pm 80)/N$. Here, $\Delta\omega$ is the difference in frequency between the desired slave laser frequency and the reference laser frequency, as given in the list above. The error signal between the reference frequency and beat signal is then put through a home-built PI loop filter. The loop filter outputs signals fed back to the slave laser, which control the laser frequency by adjusting the current and piezo-electric transducer (PZT) that moves the laser grating.

4.2 Fiber Assembly

At the heart of the experimental setup is the structure inside the vacuum chamber that holds the hollow core fiber and the various wires, coils, and optics required to

trap, manipulate, and study the atoms. Many months went into designing, machining, and assembling this structure. I really admire Misho and Vlatko's skill and patience in putting together this puzzle. The almost complete product is shown in Fig. 4-4:

Figure 4-4: Picture of fiber assembly.
MOT coils, shift coil, and quadrupole wires are shown mounted on the white MACOR structure. The fiber is held vertically in the center of the pyramid-shaped chuck, surrounded by the quadrupole wires.

The backbone of the fiber assembly is made from MACOR, a glass ceramic material that can be machined. Since we will need to quickly turn on and off the various magnetic fields involved in the experiment, using a ceramic material avoids eddy currents that are induced in metal structures. As can be see in Fig. 4-4 and 4-5, the MOT coils are wound around MACOR pieces on either side of pyramid-shaped chuck. The chuck has a square channel in the middle that holds the hollow core fiber and the four quadrupole funnel wires that run along the length of the fiber. It is then surrounded by a small coil, which we can use to provide a field in the vertical direction to shift the zero point of the MOT field to match the position of the atoms when doing magnetic trapping. The MOT lasers enter the assembly from six directions,

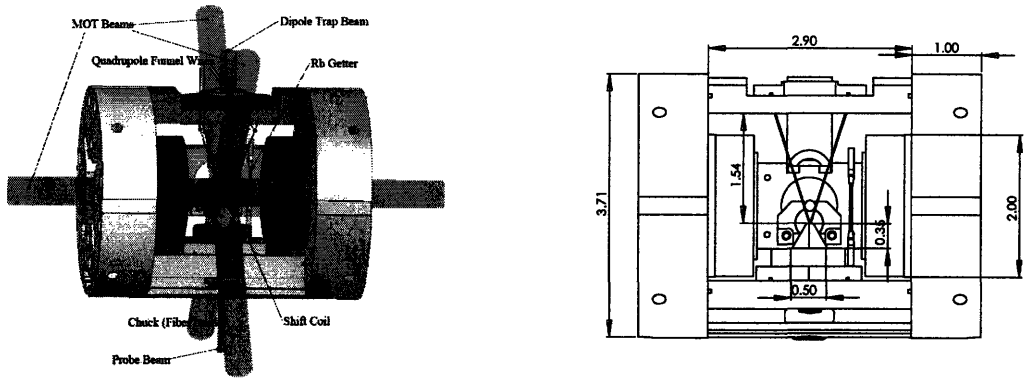

(a) (b)

Figure 4-5: Fiber assembly.
(a) SolidWorks model. Red circle between the quadrupole wires indicate the approximate position of cold atoms in the MOT. Pieces colored blue and red are used for aligning the lens used to couple light into the fiber. (b) Drawing with dimensions in inches.

forming a cloud of trapped cold atoms above the face of the fiber. In addition, there are lenses that focus the dipole and probe beams into the fiber. The lens mounts are held by MACOR pieces that can be moved and then held in place by set screws for proper alignment of the laser light. Finally, we use a rubidium getter (from SAES Getters) mounted near the MOT as our source of atoms.

4.3 Magnetic Fields

In this section, I will give calculations of the magnetic fields produced by the various coils and wires used in our setup. These calculations are important for estimating the depths of our magnetic traps and the currents that need to be provided by the controllers described in the next section.

4.3.1 MOT Coils

The transverse and axial field components of a circular single loop of current I with radius R, centered at $z = D$, $\rho = 0$ in cylindrical coordinates are given by [22, 18]:

$$B_\rho = \frac{\mu I(z-D)}{2\pi\rho\sqrt{(R+\rho)^2+(z-D)^2}}\left[-K(k^2)+\frac{R^2+\rho^2-(z-D)^2}{(R-\rho)^2+(z-D)^2}E(k^2)\right], \quad (4.2)$$

$$B_z = \frac{\mu I}{2\pi\sqrt{(R+\rho)^2+(z-D)^2}}\left[K(k^2)+\frac{R^2-\rho^2-(z-D)^2}{(R-\rho)^2+(z-D)^2}E(k^2)\right], \quad (4.3)$$

where the the arguments of the complete elliptic integrals K and E is [19]

$$k^2 = \frac{4R\rho}{(R+\rho)^2+(z-D)^2)}. \quad (4.4)$$

Here, μ is the permeability of free space $\mu_0 = 4\pi \times 10^{-7}$, and $B_\phi = 0$. For an anti-Helmholtz configuration, we add another loop at $z = -D$, $\rho = 0$ with current flowing in the opposite direction. Expanding to third order, the total field components are:

$$B_\rho = \mu I\left[-\frac{3}{2}\frac{DR^2}{(D^2+R^2)^{5/2}}\rho+\frac{15}{16}\frac{R^2(4D^2-3R^2)}{(D^2+R^2)^{9/2}}(\rho^3-4\rho z^2)+\ldots\right], \quad (4.5)$$

$$B_z = \mu I\left[3\frac{DR^2}{(D^2+R^2)^{5/2}}z+\frac{15}{24}\frac{R^2(4D^2-3R^2)}{(D^2+R^2)^{9/2}}(4z^3-6\rho^2 z)+\ldots\right]. \quad (4.6)$$

The second order terms from the two coils cancel, and the field is linear in both z and ρ to first order, as mentioned in the previous chapter. Each MOT coil has 30 turns, and therefore has a certain width and thickness, but we can estimate the field by pretending all the turns are at some average position. The average radius is $R = 2.2$ cm and the separation between the coils is $2D = 4.3$ cm. Using these parameters, the exact field components and gradients along their corresponding directions are plotted in Fig. 4-6 for a current of 5 amps.

4.3.2 Bias Coils

The bias coils are used for a variety of purposes, including canceling background fields, optical pumping, and shifting the magnetic trap provided by the MOT coils.

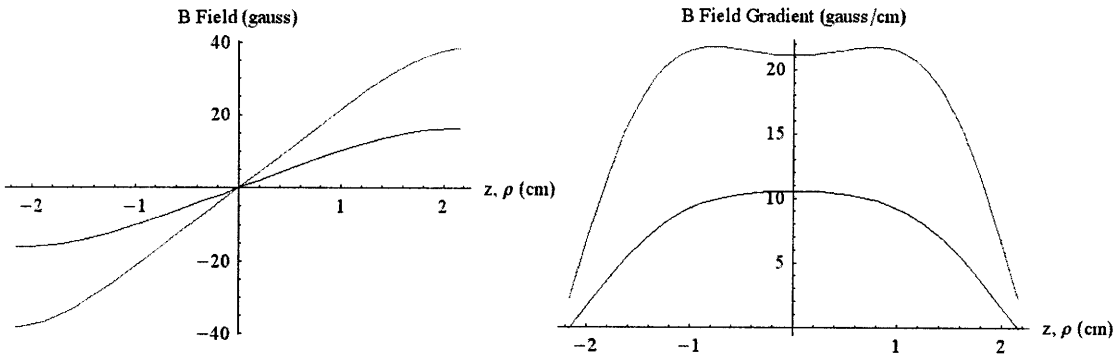

Figure 4-6: Magnetic field components and gradients for the MOT coils
B_z is plotted along z ($\rho = 0$) in red and B_ρ is plotted along ρ ($z = 0$) in blue. The z direction gradient is twice the ρ direction gradient.

These processes will be described in more detail in chapter 6, but in general, we need the bias coils to provide a homogeneous magnetic field. This is done by three pairs of rectangular coils in the x, y, and z directions, as shown in Fig. 4-7. Here, z is defined along the axis of the MOT coils, y is in the vertical direction, and x is the other third perpendicular direction. The x and y direction coils have outer side lengths of 4 inches and a 0.5in×0.5in cross section. They are separated by 8.5 inches at the center. The z direction coils have outer side lengths of 11 inches with the same cross section . They are lined up with the edges of the x and y coils, and are therefore separated by 3.5 inches at the center. The small coils x and y coils have 86 turns, and the large z coils have 30 turns.

We can calculate the fields using the equations given in [20]. For a square coil in the $x-y$ plane centered at the origin, with side length L parallel to the x and y axes, the z component of the magnetic field at a point (x, y, z) is

$$B_z = \frac{\mu I}{4\pi} \sum_{k=1}^{4} \left[\frac{(-1)^k d_k}{r_k(r_k + (-1)^{k+1} C_k)} - \frac{C_k}{r_k(r_k + d_k)} \right], \tag{4.7}$$

where

$$C_1 = -C_4 = L/2 + x, \qquad d_1 = d_2 = y + L/2,$$
$$C_2 = -C_3 = L/2 - x, \qquad d_3 = d_4 = y - L/2,$$

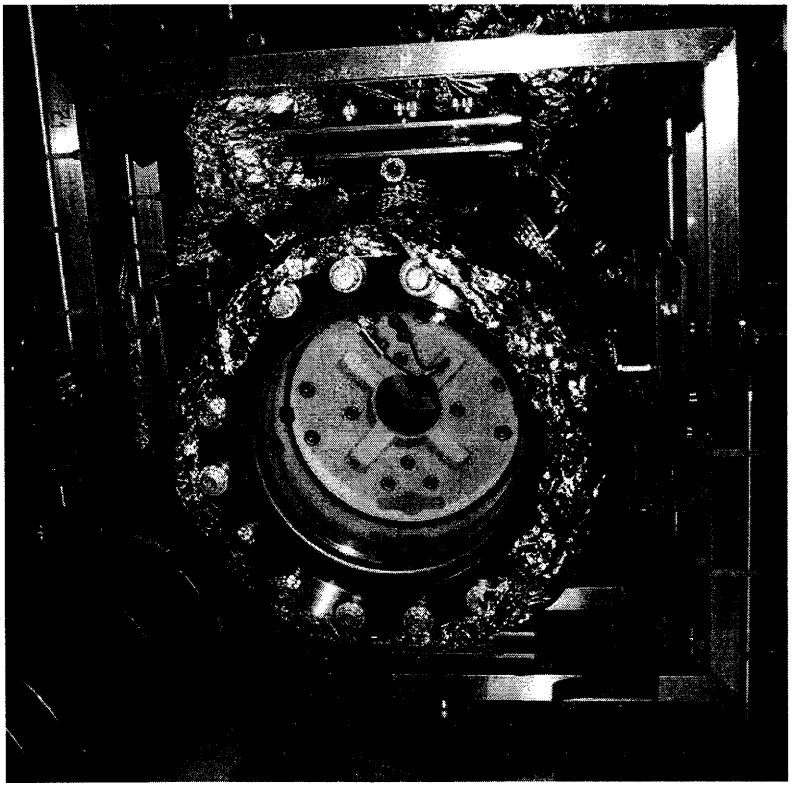

Figure 4-7: Picture of bias coils and vacuum chamber.
We are looking down the z axis of the setup. The vertical direction is y.

and the distance from the four corners are

$$r_1 = \sqrt{(L/2+x)^2+(y+L/2)^2+z^2}, \qquad r_2 = \sqrt{(L/2-x)^2+(y+L/2)^2+z^2},$$
$$r_3 = \sqrt{(L/2-x)^2+(y-L/2)^2+z^2}, \qquad r_2 = \sqrt{(L/2+x)^2+(y-L/2)^2+z^2}.$$

Using a similar geometry as the MOT coil calculations, we put one coil at $z = D$ and another at $z = -D$ (which just replaces z by $z \pm D$ in the above equations). Unlike the anti-Helmholtz MOT coils, however, the currents here run in the same direction. The expansion for the fields at the origin are given in [22] and are quite messy. However, the important result is that there is a zeroth order term in the axial field B_z is given by

$$B_z = \frac{4\mu I L^2}{\pi(D^2+L^2/2)^{1/2}(4D^2+L^2)} \tag{4.8}$$

and second order terms that vanish when $2D \approx 0.544506L$. Our bias coils are not in this perfect Helmholtz configuration, so we need to make sure that the gradients are not significant. Otherwise, in addition to providing a homogeneous field, the gradients from the bias coils would interfere with that of the MOT coils and quadrupole funnel wires. Fig. 4-8 gives the axial fields of the bias coils with the field at the origin set to 1 gauss. This requires 0.55 amps of current for the big coils, and 0.62 amps of current for the small coils. For typical operating parameters, the additional gradient

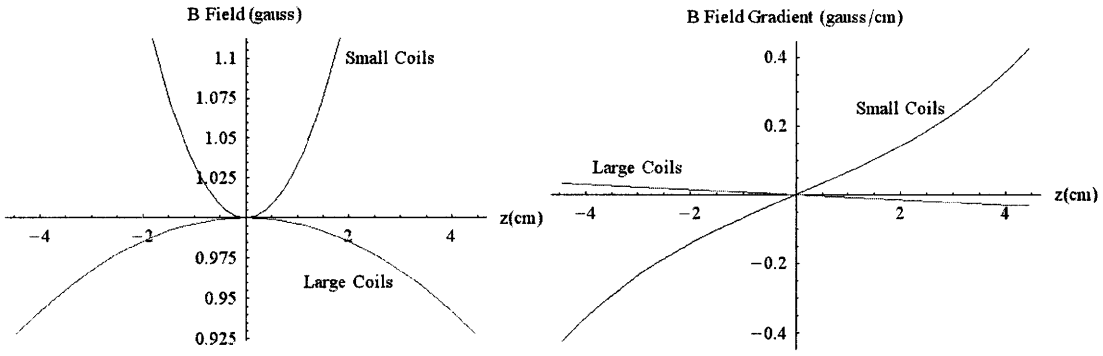

Figure 4-8: Magnetic field and gradient for the bias coils
The axial field B_z and the gradient dB_z/dz is plotted for both the big and small bias coils, for which the axial direction corresponds to the x, y, and z directions of the setup. The field of the big coils has a maximum at the origin since the separation is slightly less than optimal (2D/L=0.33). The field of the small coils has a minimum and a higher gradient since the separation is much larger than optimal (2D/L=2.43).

of the bias coils is less than 1% of the gradient provided by the MOT coils. As we will see later, the bias coils end up being used for a variety of other purposes. However, the gradient caused by the deviation from Helmholtz configuration never becomes a major concern.

4.3.3 Quadrupole Funnel Wires

There is unfortunately no handy expression for the field of the quadrupole funnel wires, and so we calculated the field by dividing the wires into small elements and

summing the contributions as given by the Biot-Savart law,

$$d\vec{B} = \frac{\mu_0}{4\pi}\frac{Id\vec{l}\times\hat{r}}{r^2}, \tag{4.9}$$

Here I is the current, $d\vec{l}$ is the length vector of the current element, and $r\hat{r}$ is the displacement vector from the current element to the field point. Fig. 4-9 shows the geometry of the wires along with the axes defined for the setup and used in the plots below. Inside the chuck, the four wires run parallel next to each other with the fiber

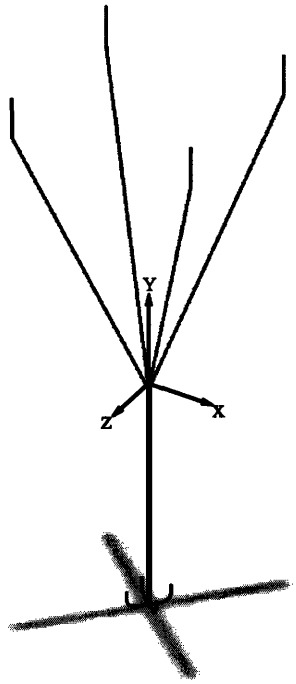

Figure 4-9: Quadrupole funnel wires.
The fiber is sandwiched between the four wires along the negative y axis.

tucked in the middle and are separated by 280 μm, which is just the wire diameter. Above the fiber, they fan out and are separated by 2.5 cm at the top MACOR bar, which is a height of 3.9 cm from the top of the chuck. Fig. 4-10 shows the magnitude of the field produced by the wires for 1 amp of current. We find that the gradient of the magnetic field is 11 gauss/cm/A along the x and z directions at a distance y=6 mm above the fiber, which is where the MOT is formed. This increases to 1800

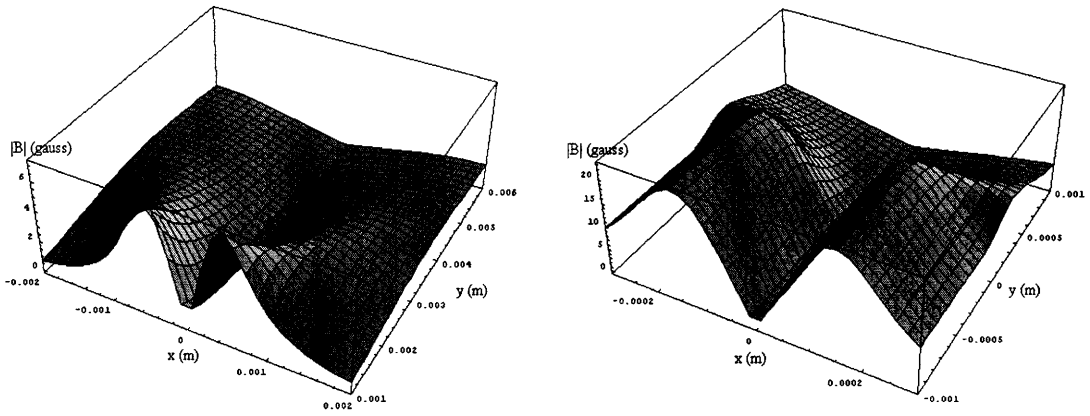

Figure 4-10: Magnetic field of the quadrupole funnel wires.
The field magnitude is plotted for the z=0 plane. Recall that y is the vertical direction and y=0 is the top of the chuck where there is a kink in the wires. The left plot shows the field starting from 1mm above the chuck, and the right plot shows the field inside the chuck. The ridges in the magnitude correspond to the positions of the wires.

gauss/cm/A at y=0 near the top face of the fiber.

The fourth source of magnetic fields we use is the shift coil around the chuck that holds the fiber. Since it is just used for small adjustments of the MOT field in the y direction at the beginning of magnetic trapping, it's not so important to know the exact shape of the field everywhere. I will just mention here that the y direction field generated at the MOT is ~2 gauss per amp. The largest field we need is ~4 gauss, so even though there is only one coil, the gradients generated is less than 10% of the gradient from the MOT.

The calculations here provide us with a rough idea of what kind of fields and gradients can be generated. These estimates of the generated fields, along with other considerations such as the heating and resistance of the coils, then dictate the design of controllers used to provide current to each set of coils and wires. These are the subjects of the next chapter. In practice, the actual sequence of currents used in the experiment is determined through trial and error. Many things change from the original plan we had in mind when designing the coils and controllers. For example, as described in chapter 6, some coils will end up providing more field than originally intended. Therefore, it is good to have an idea of the capabilities of our design.

Chapter 5

Current Controllers for Generating Magnetic Fields

Each of the magnetic coils and wires described in the previous chapter have different requirements in terms of the strength and timing of the fields they need to generate, so individual current controllers had to be designed for each one. As you will see in the last section, we often ended up using the controllers for things other than what we originally intended, but this section gives the initial motivations for the designs. First, I will briefly describe the common aspects of all three controllers.

5.1 PI Feedback Circuits

Although the details differ for each current controller, the essential scheme is the same for all three. In all of our controller systems, the current through the coils is provided by a voltage controlled current source (such as a MOSFET, which I will use as the example in this section) driven by a proportional-integral (PI) feedback circuit. The feedback circuit serves to control and stabilize the voltage applied to the gate of the MOSFET, which determines the drain-to-source current. Here, I give a general picture of how a PI controller works, but more details on signal processing and control theory can be found in books such as [21]. An external control signal, which in our case may be a voltage applied using a potentiometer, signal generator, or computer output

determines the nominal current we want to drive through the system. An op-amp summing junction takes the difference between this signal and the voltage measured by a current sensing resistor connected in series with the MOSFET and coil. A PI compensator implemented using another op-amp takes this error signal and produces the necessary voltage to make it go to zero. This is done through a proportional gain, which takes into account the instantaneous error, and an integrator, which includes information about the error in the past. For example, if the voltage measured across the current sensing resistor is smaller than the control voltage, the PI stage will output a larger voltage to the MOSFET gate, thus increasing the current and the measured voltage. The stability of the feedback loop and how quickly it responds to changes in the error signal are characterized by two parameters, the gain and the corner frequency ω_c. The gain controls how dramatically the PI output responds to the error signal input. In most cases, setting the the gain too high causes instability and oscillations in the system, while setting it too low increases the response time. The corner frequency controls the range of frequencies in the error signal to which the system responds. A large corner frequency decreases the response time, but filters out noise at a smaller range of frequencies. The effects of these two parameters can be illustrated through a bode plot of the system. The transfer function of a PI controller is

$$G(s) = \frac{v_{out}(s)}{v_{in}(s)} = K_p + \frac{K_i}{s} = \frac{K_i(1+\tau_i s)}{s}, \tag{5.1}$$

where $\tau_i = K_p/K_i$ is $1/\omega_c$. In our case of an op-amp PI circuit as shown in Fig. 5-1, $K_p = R_{cf}/R_g$, $K_p = 1/R_g C$, and $\omega_c = 1/R_{cf}C$. A bode plot for typical values of resistors and capacitor used in the controller for the bias coils is given in Fig. 5-2. While these are the general effects of these two parameters, the actual behavior of the circuit depends greatly on factors such as the linearity of the MOSFET response and the electronic noise present. Although it's good to have a general idea of which way to adjust the parameters to improve the output signal, in the end, I often find myself fine tuning the R_g and R_{cf} based on the output signal I see on the oscilloscope.

While the PI feedback control the underlying scheme, the variations and extra

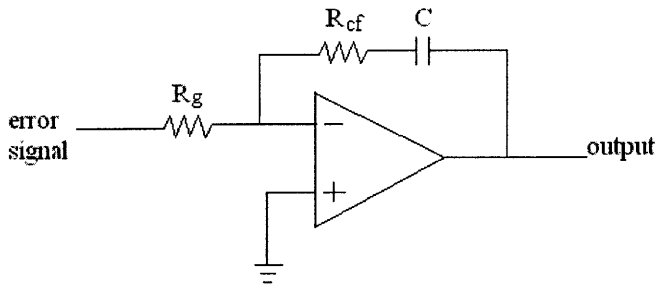

Figure 5-1: PI compensator using op-amp.

features that are involved in both the circuit and everything else that goes in the current controller box depend on the specific requirements of the system. Some general issues that arise include those involved in driving inductive loads and heating of the MOSFETS, current sensing resistors, etc. We deal with these issues in the design of the three different current controllers described below.

5.2 The Bias Coil Controller

I will start with the controller for the quadrupole wires since it is the most straightforward in design (see A-1 in Appendix A for a schematic diagram and A-2 for the board layout). Each printed circuit board contains two PI controllers, so three boards were used to control all six bias coils, as shown in Fig. 5-3. The initial purpose of bias coils was to cancel background fields, which would require a constant current of ~0.5 A for a 1 gauss field. In addition, we use the coils in the y direction to move the zero of the magnetic trap, which would require pulses of higher currents. The feedback is initially optimized for a DC current of 0.5A with 10ms pulses at 1Hz to 3A (1% duty cycle) while making sure the system was stable up to 6A pulsed. Optimizing the feedback involves tuning R_g and R_{cf} to ensure stability and minimize the rise time of the current response. For ease of reference, I list here some useful information for the bias coil controller for the initial optimization. Note that the voltage of the power supply is $I(R_{load} + R_{sense}) + V_{DS}$, where V_{DS} is the drain-to-source voltage of the MOSFET and R_{load} is 2.5Ω for the bias coils. This was set to the lowest voltage that

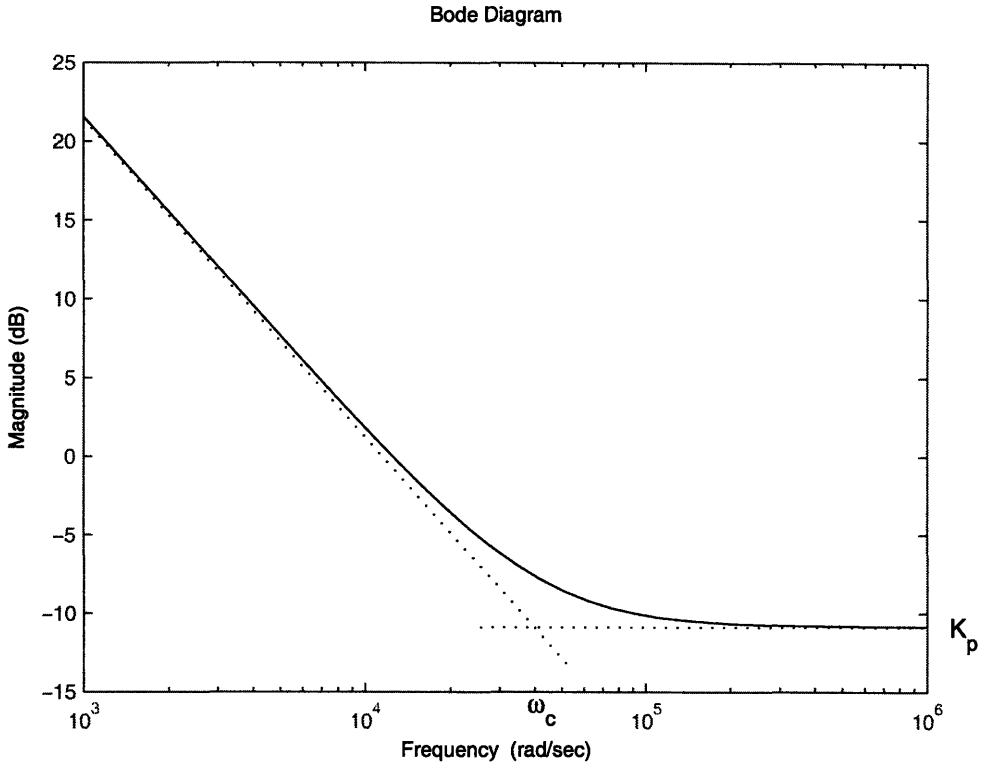

Figure 5-2: Bode plot for a PI compensator used in the bias coil controller. Here, $R_g = 8.33\text{k}\Omega$, $R_{cf} = 2.38\text{k}\Omega$, and $C = 10\text{nF}$, giving $K_p = 0.28 = -11\text{dB}$ and $\omega_c = 42\text{kHz}$.

allowed MOSFET operation in the saturation regime to minimize power dissipation and heating of the MOSFET. It will have to be increased for pulsing greater currents or for a larger load resistance.

- Current Source: International Rectifier IRFB23N15D MOSFET (23A 150V)
- Output Current: $I = V_{control} * 4A/V = V_{monitor} * 2A/V$
- Power Supply Voltage (for 6A): 17V
- Rise Time (for 3A pulse with $100\mu s$ input edge time): $350\mu s$ (x and y coils), $250\mu s$ (z coils).

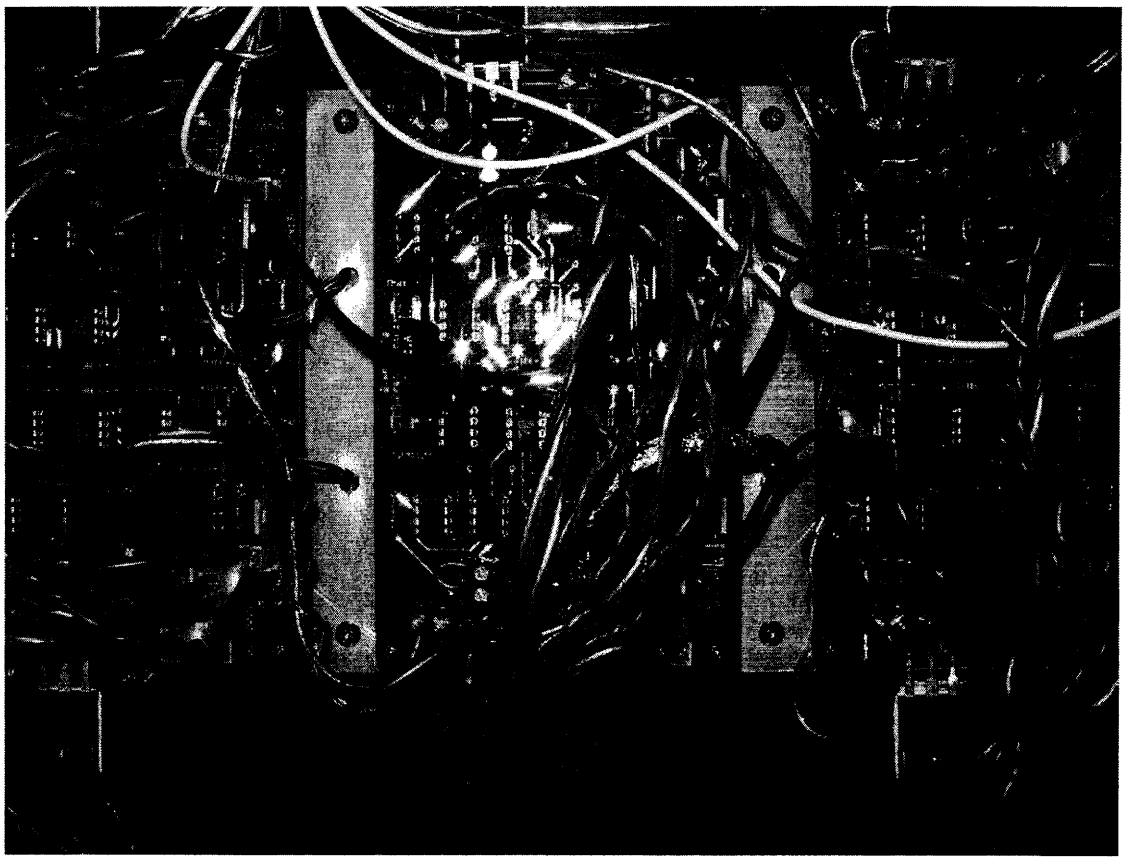

Figure 5-3: Current controllers for the bias coils.

5.3 The Quadrupole Wires Controller

The controller for the quadrupole wires (Fig. A-3 and Fig. A-4) is similar to bias coil controller. The main additional concern is that we will need to pulse currents up to 8A for ~40ms every second, which leads to high power dissipation and heating of the components. To resolve this issue, we separated the high current path from the printed circuit board. As can be seen on the schematic, only the MOSFET gate-to-souce voltage and the voltage across the current sensing resistor are connected to the board, thus ensuring that no high current flows on the board itself. A high power MOSFET was tested for pulsing currents up to 20A.

While burning MOSFETS are causes for concern, a bigger problem is the heating of the quadrupole wires themselves. Because they are in vacuum, there is very little heat dissipation except through the connections to the ends of the wires. Significant

heating of the wires will damage the Kapton insulation, and anything going awry would require opening the vacuum and replacing the wires, which is a huge task. Therefore, we had to take extra precautions to prevent overheating. First, we got a general idea of the heating in the wires by testing the current controller on 40 inches of $120\mu m$ wire outside of the vacuum, which is the same as the total length of wire actually used. While the rate of heat dissipation will be different, we were mostly interested in the temperature change during the pulse of high current. This gives the wire relatively little time to thermalize with the environment anyway, so the effect of not being in vacuum is not so significant. In addition, the wires inside vacuum are individually connected on both ends to thick copper wires outside the feedthroughs, which should provide a good heat sink. We measured the temperature change of the wires by finding the voltage drop across it while pulsing the current, which tells us the resistance. The temperature increase is then given by

$$\Delta T = \frac{R/R_0 + 1}{\alpha}, \tag{5.2}$$

where R_0 is the resistance at room temperature and $\alpha = 3.9 \times 10^{-3}\ ^oC^{-1}$ is the temperature coefficient of resistance for copper. R_0 was measured through the voltage drop at the beginning of a 10ms 1A pulse. The results are shown in Fig. 5-4. As a conservative limit, we set the maximum temperature allowed for the wire to be 80°C. Even at 20A, for example, this lets us pulse the current for 30ms, which is enough time to magnetically trap the atoms while they are transferred to the dipole trap. To set this limit, we simply found an appropriate fuse and put it in series with the wires. After connecting the controller to the actual wires in vacuum, we measured the temperature of the wires using the same method and found that the heating was comparable to our measurements outside of vacuum. As an extra precaution, the input to the quadrupole wire current controller is directly programmed into a signal generator, which is synchronized with the rest of the timing sequence by triggering from the computer. Compared to direct input from a computer, it is now much harder to, say, accidentally increase the pulse length by while changing other things in the

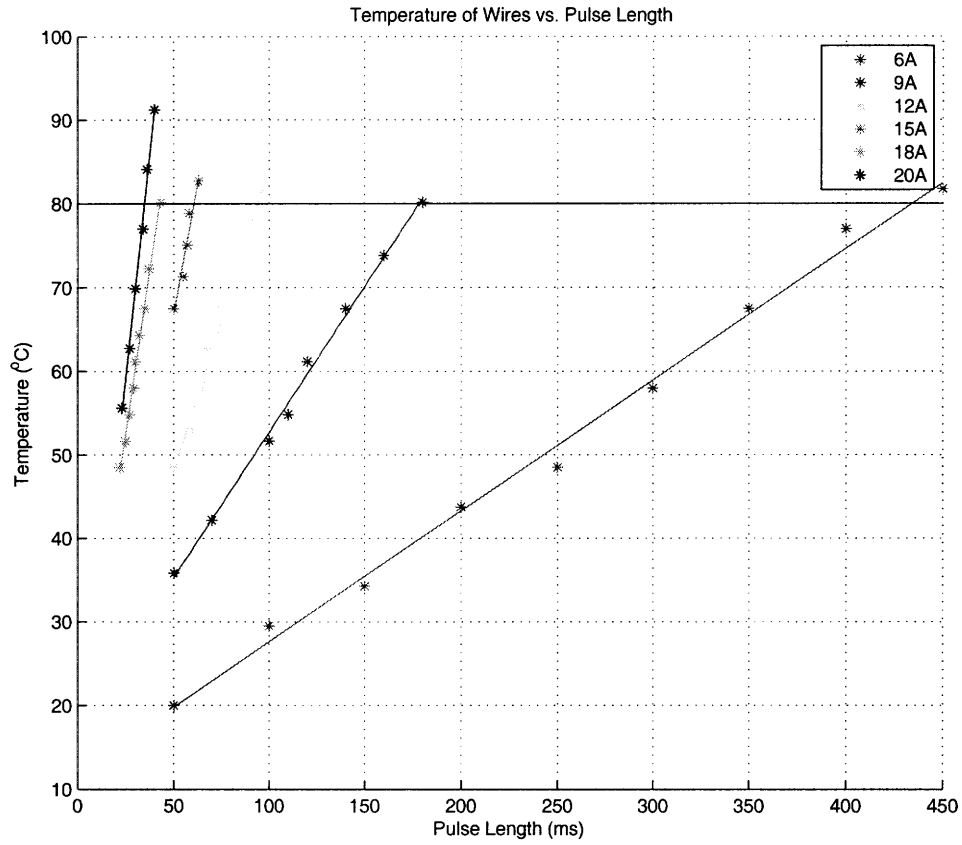

Figure 5-4: Dependence of wire temperature on pulse length and current. Horizontal line at 80°C is our set temperature limit.

control sequence.

Here is some useful information for the quadrupole wire controller:

- Current Source: IXYS IXFN120N20 MOSFET (120A, 200V)
- Output Current: $I = V_{control} * 10A/V = V_{monitor} * 5A/V$
- Power Supply Voltage (for 20A): 16V
- Rise Time (for 15A pulse with $100\mu s$ input rise time): $200\mu s$ (This may have changed as the feedback is re-optimized for different currents over time).
- Fuse: 3A ATO
- MOSFET Temperature (15A, 3% duty cycle): 25°C

5.4 The MOT and Shift Coil Controller

In our original design for the MOT and shift coil controllers, we wanted a bipolar current source that could be used to reverse the current briefly after turning off a pulse to cancel eddy currents induced in the metal vacuum chamber. The circuit (Fig. A-5 and Fig. A-6) is based a design described in [22] and uses a pair of high power opamps (TI OPA549) that drive the coil between floating outputs. The signal from the PI output, which is added to a center point voltage V_{cp}, controls the difference in current of the two opamps, and one acts as the source of the current while the other acts as the sink. The output voltage of the opamps are given by $V_{\pm}$ =gain$\times(V_{cp} \pm V_{PI})$, where the gain is given by $1 + R10/R12$ in the top opamp in the schematic (and similarly for the bottom opamp). To use the full range of the power supply voltage V_s and have a symmetric range of control for positive and negative current, we set $V_{cp} = V_s/2/\text{gain}$ using the potentiometer R4.

The advantages of this design are that, unlike bipolar controllers made with MOSFETS, the power opamps are linear throughout throughout the operating range, including when crossing zero current. In addition, this configuration ensures that an control input of 0V corresponds to zero current even if the opamps themselves have an offset and the gains are not exactly equal, since they will both be outputting the same current. Another useful feature of the OPA549 is the E/S pin, which can be pulled low to disable the output through a switch (MAXIM MAX319CJA). Not only is this good for rapidly switching off the current without going through the PI control, the opamp has an internal temperature monitor pulls this pin low if it overheats.

Due to the large inductance of the MOT coils, we had to add a 1Ω resistor in series with the coil to decrease the rise time. For a $10\mu s$ input pulse rise time, this decreased the output rise time by about a factor of two. Of course, since we will be running 8 amps of CW current through the system, the resistor must be properly heat sunk. Even though the quadrupole wire controller has to pulse to larger currents and initially caused much more trouble with overheating, there is negligible heating in the final design after switching to a very high power MOSFET. For the MOT coil

controller, overheating can still be a problem, and we measured the temperature of various components and on-board traces in the high current path while running 7A DC current (the maximum current that can be supplied by the opamps is 8A). As can be seen in Table 5.1, there is significant heating of the opamps and 1Ω resistor, and care should be taken if the current needs to be pushed higher.

Part	OPA549(1)	OPA549(2)	0.1Ω R(1)	0.1Ω R(2)	R_{sense}	1Ω R	Traces
Temp.(^{o}C)	57	69	38	42	35	64	34

Table 5.1: Temperatures of various high current path components of MOT current controller after running 7A for 45min.
OPA549(1) and 0.1Ω R(1) are closer to the fan, and therefore have lower temperatures than their duplicate on the other side of the board.

The controller for the shift coil is set up identically to the one for the MOT coil. Below are some initial settings for the MOT coil controller. Note that if a different V_s is used than in the list below, the center point voltage should be set accordingly.

- Current Source: Texas Instruments OPA549 (-8A to 8A)
- Output Current: $I = V_{control} * 5A/V = V_{monitor} * 5A/V$
- Power Supply Voltage (for 8A): 18V
- Center Point Voltage: 5V
- Rise Time (for 7A pulse with $10\mu s$ input rise time): $250\mu s$ (Note: This was tested with a coil that was comparable to *one* MOT coil, and may be different for two coils in series or for the shift coil).

Chapter 6

Timing Sequence and Results

Currently, the procedure and setup of the experiment are still changing almost every day. We have loaded atoms into the dipole trap, and are exploring ways of studying their behavior in the trap and determining the number of atoms in the fiber. What *has* become relatively stable is the procedure for capturing the MOT and transferring the atoms to the dipole trap, so I can discuss the that part of timing sequence we are currently using and show what the atoms are doing at different steps of the process. I will include at the end some preliminary evidence of captured atoms in the dipole trap, but what happens after that point is a work in progress.

6.1 Timing Sequence

Fig. 6-1 shows the sequence of magnetic fields and lasers used to trap and transport the Rb atoms to the fiber. Before the start of this sequence, the MOT coils and lasers are turned on for 800 ms to trap and cool the atoms. While collecting the MOT, 3 amps of current is run through the coils, generating a gradient of 6 g/cm in the x-y plane and twice of that in the z direction. The trapping beams are detuned 20 MHz from the $F = 2 \rightarrow F' = 3$ transition. The MOT field is then increased to 24 g/cm to compress the cloud of atoms. 20 ms into this compression, the MOT beams are further detuned to 140 MHz from the transition to prepare for polarization gradient cooling. The MOT fields are turned off after 50ms, while cooling continues with the

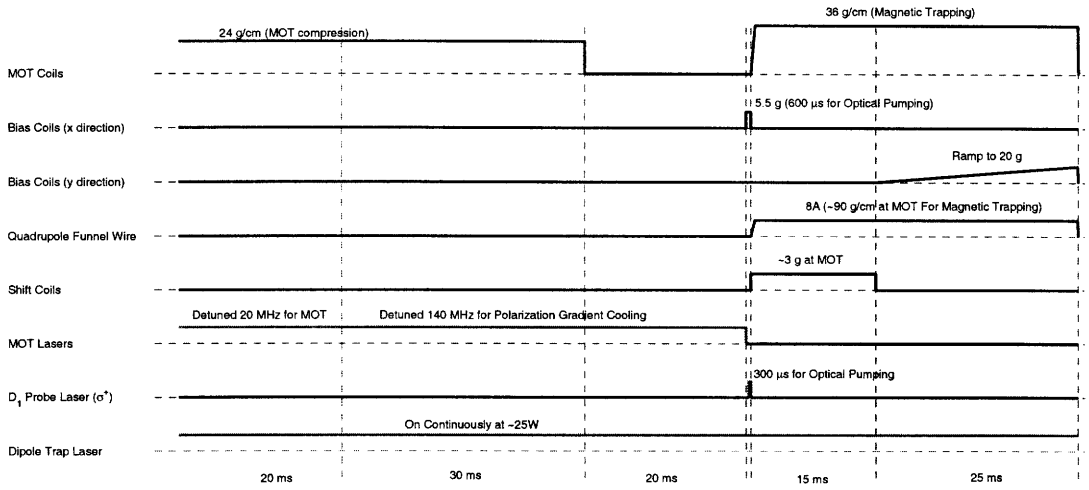

Figure 6-1: Timing sequence of magnetic fields and lasers
The MOT coils and lasers are on for 800 ms to collect atoms in the MOT before this sequence starts. The heights of the pulses are arbitrary, but are labeled with the relevant values. The z direction bias coils are currently not used in the experiment.

MOT lasers for another 20 ms.

After the MOT lasers are turned off, we prepare the atoms for magnetic trapping by optical pumping them into the $F = 2, m_F = 2$ ground state. This is done by applying a field of 5.5 gauss with the bias coils in the x direction to Zeeman split the m_F states. 600 μs after the field is turned on, we add a σ^+ polarized probe beam on resonance with the D1 $F = 2 \rightarrow F' = 2$ transition. Since this beam cannot couple the $F = 2, m_F = 2$ state to an excited state, the atoms will eventually be optically pumped to the desired ground state. We turn off the bias coils and laser used for optical pumping 300 μs after the beams are turned on.

At this point, we begin to ramp up the field from the MOT coils to provide a trapping potential in the vertical y direction and the quadrupole funnel wires for the x and z directions. The MOT coils must provide at least enough gradient to trap the atoms against gravity. Setting the trapping force equal to the force due to gravity, we need a gradient of

$$\frac{dB}{dy} = \frac{mg}{\mu} = 15 g/cm, \tag{6.1}$$

where m is the mass of a ^{87}Rb atom, and $\mu = \mu_B g_F m_F$. However, we really want to just make the trap as deep as possible to capture atoms with higher temperatures. We currently provide a gradient of 36 g/cm, which corresponds to 18 amps of current. Here, we are limited by the heating of the coils at such high currents. Also note that, since the current controller originally designed for the MOT coils can only supply 8 amps, we ended up using one of the bias coil controllers to drive the MOT coils. We provide additional confinement in the horizontal directions by driving 8 amps through the quadrupole funnel wires. This gives a gradient of ~90 g/cm at the position of the MOT, and increases near the fiber as shown in section 4.3.3. These fields take about 500 μs to turn on, after which we allow the atoms to thermalize for 15 ms. During this time, we adjust the zero the y direction potential to coincide with the position of the atoms using the shift coil. The MOT lasers are currently aligned such that the atoms are collected about 1mm above from the true zero of the MOT field. If we do not adjust the position of the minimum of the potential, the atoms will gain energy and heat up as they fall due to gravity before they are trapped. Given the gradient of the MOT coil, we need to provide a field of 3 to 4 gauss with the shift coil. The shift coil is controlled with the bipolar current controller, which allows us to provide a current in the opposite direction if the lasers become aligned such that the field needs to be shifted down instead of up.

After the atoms have thermalized, the shift coil is turned off and we begin to ramp up the field provided by the bias coils in the y direction. This adiabatically brings the atoms toward the fiber by shifting the zero of the trapping potential. Since the field gradient in the y direction is 36 g/cm, and the MOT is collected 6mm above the fiber, we increase the bias coil fields to ~20 gauss in 25 ms to bring the atoms to the face of the fiber. If all goes well, the atoms are now delivered to the dipole trap, which remain on for the duration of the experiment.

6.2 MOT Atom Number and Temperature

After polarization gradient cooling, we estimate the number of atoms in the MOT to be on the order of 10^6 and the temperature to be between 30 and 40 μK. These estimates were made using absorption images taken with a CCD camera, such as Fig. 6-2. The temperature was estimated using a time-of-flight measurement. We look

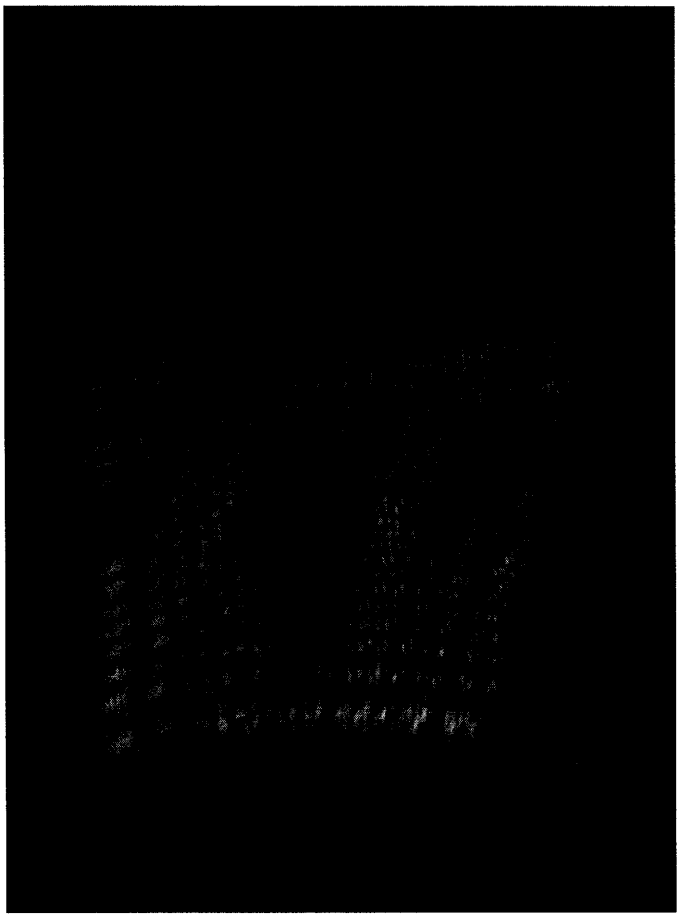

Figure 6-2: Absorption image of atoms in the MOT immediately after polarization gradient cooling.
We are looking down the x axis of the setup. The size of the atom cloud in the horizontal (z) direction is ~0.8mm and about twice of that in the y direction. The dark profile is the MACOR and the edge of a focusing lens.

images at 1 ms intervals after the end of polarization gradient cooling and subtract them from a background image taken without the MOT. Due reflection of the lasers from the MACOR, the intensity of the background image is approximately given by

$I_{bkg} = I_0 + I_D$, while the intensity of the MOT image is given by $I_{MOT} = I_0 e^{-d} + I_D$, where d is the optical depth of the cloud. These expressions are not quite correct, since there is also an oscillating interference term between the light that passes through the atoms and the light that is reflected from the MACOR. For an estimate of the temperature, however, we ignore that term for now and assume a Gaussian distribution of atoms. The subtracted image then has an intensity profile along the vertical and horizontal directions given by

$$I = I_0 \left[1 - exp\left(-d_0 e^{-\frac{(x-x_0)^2}{r^2}}\right)\right]. \tag{6.2}$$

As described in [23], the most probable radius of the cloud in a particular direction changes in time as $r^2 = r_0^2 + v_0^2 t^2$ after the trap is turned off, where $v_0 = \sqrt{2kT/m}$. By fitting for r at different times and then finding v_0, we can determine the temperature of the atoms.

6.3 Magnetic Trap Statistics

We also estimated various properties of the atoms magnetically trapped in the funnel produced by the quadrupole wires. This was done using pictures taken at different times during the process of lowering the atoms toward the fiber, such as the one shown in Fig. 6-3. To analyze these images, we first divide them by a background image taken without the atoms to get $I/I_0 = e^{-d}$, which then gives us the position dependent optical density $d(y,z) = \sigma_0 n(y,z)$, where σ_0 is the atomic scattering cross section and $n(y,z)$ density of atoms per unit area, since the x direction is already integrated out in the picture. We then take horizontal slices of $d(y,z)$ with height Δy and find the average $d(z) = \sigma_0 \int n(y,z)dy/\Delta y$ within each slice. Fitting $d(z)$ to a Gaussian of the form

$$d(z) = ae^{-\frac{(z-z0)^2}{w^2}} \tag{6.3}$$

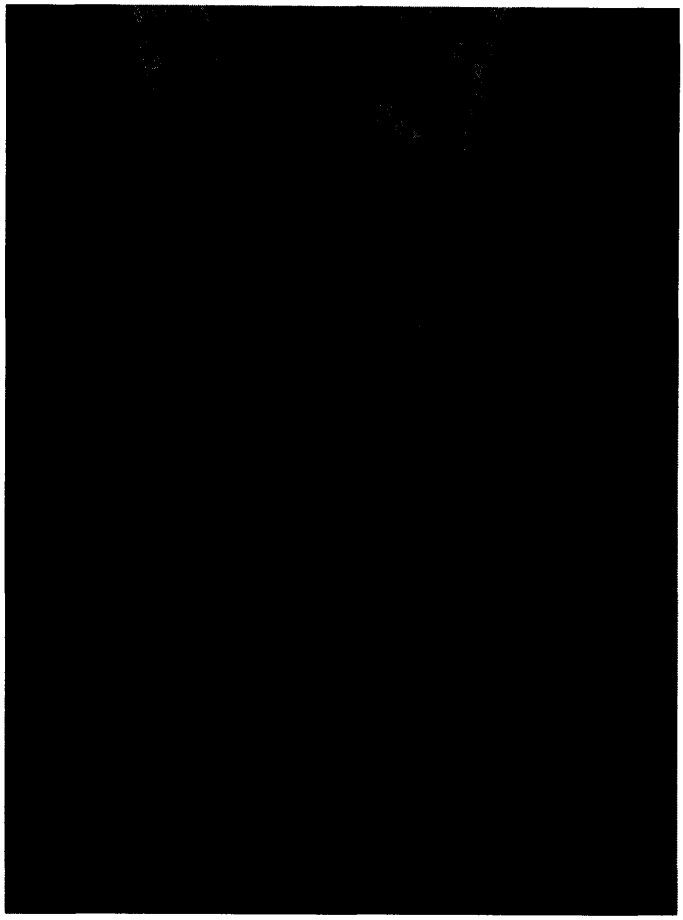

Figure 6-3: Absorption image of atoms in the funnel trap.
The dark profiles are the quadrupole wires. The shadow in the middle is due to absorption by atoms.

gives the total number of atoms in the slice as

$$N_{slice} = \int\int n(y,z)dydz = \sqrt{\pi}aw\Delta y/\sigma_0, \tag{6.4}$$

where the integral is over the area of the slice. Actually, the distribution of atoms are not quite Gaussians, possibly because the atoms have not had time to thermalize as they are moved through the funnel. Nevertheless, the fit gives us a reasonable estimate of the number of atoms and the width w of the distribution, from which we can then calculate a number of other useful quantities. First, the density D is the

total number atoms divided by the volume of the slice, which is just

$$D = \frac{N}{\pi w^2 \Delta y}. \tag{6.5}$$

Next, we can estimate the temperature of the atoms using the magnetic fields of the quadrupole wires found in section 4.3.3. Since we are considering a roughly two-dimensional slice of atoms, the average kinetic energy is given by <KE>=k_BT, where k_B is Boltzmann's constant and T is the temperature. This is then related to the potential energy of the atoms in the magnetic trap by the Virial Theorem:

$$\mu_B B = 2k_B T \Rightarrow T = \frac{\mu_B w}{2k_B}\frac{dB}{dz}. \tag{6.6}$$

Finally, we can calculate the phase space density of the atoms as

$$\rho = D\left(\frac{2\pi\hbar^2}{mk_B T}\right)^{3/2} \tag{6.7}$$

These quantities are plotted versus the distance from the fiber for different times during the transfer process in Fig. 6-4. The total number of atoms in the funnel is found by summing over the slices, and the total optical depth along the y direction is given by

$$d_{total} = \sigma_0 \Delta y \sum_{slices} D. \tag{6.8}$$

These are plotted versus time in Fig. 6-5. At the beginning of the transfer process (143 ms, with respect to some t=0 in the timing sequence), all the atoms are above the funnel. The number of atoms increases as the cloud is lowered and then decreases again as many of the atoms are slammed against the fiber and lost. The temperature of the atoms increase as they approach the fiber, which limits the number of atoms that can be loaded into the dipole trap.

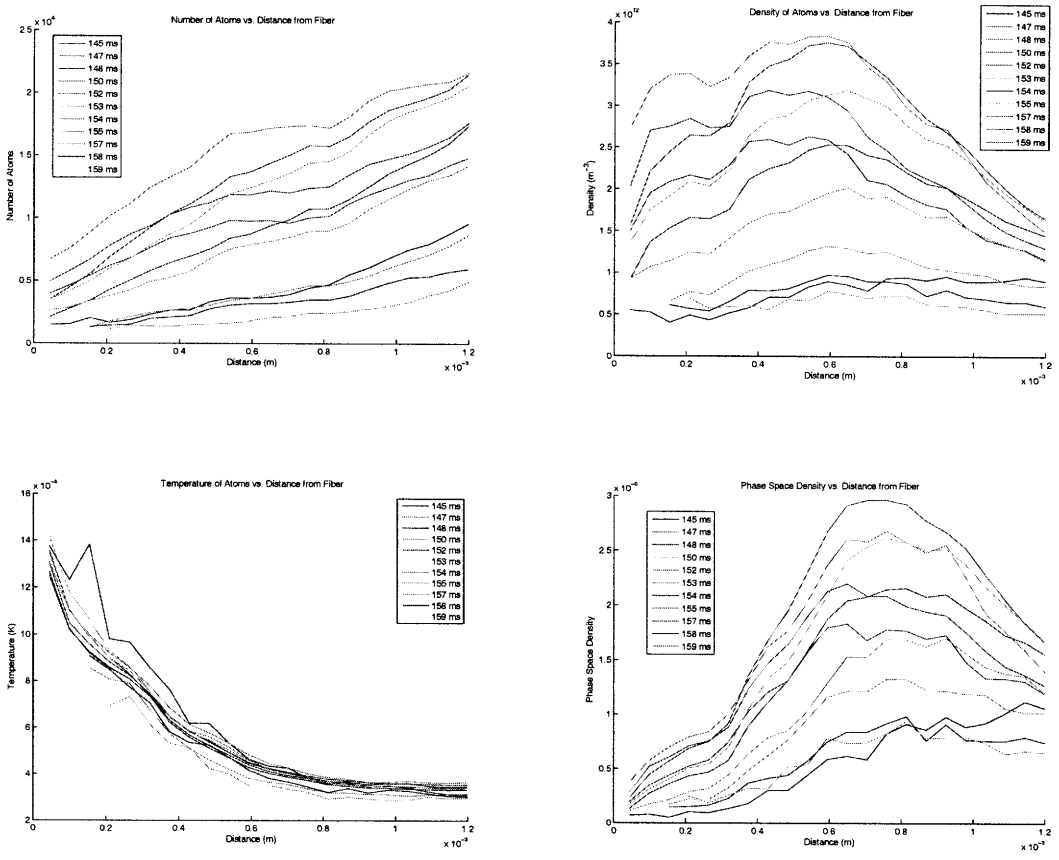

Figure 6-4: Properties of funnel trapped atoms

The number of atoms, density, temperature, and phase space density for each slice are plotted against the distance of the slice from the fiber. Several slices close to the fiber were discarded for the last three times because the low statistics did not allow proper fitting.

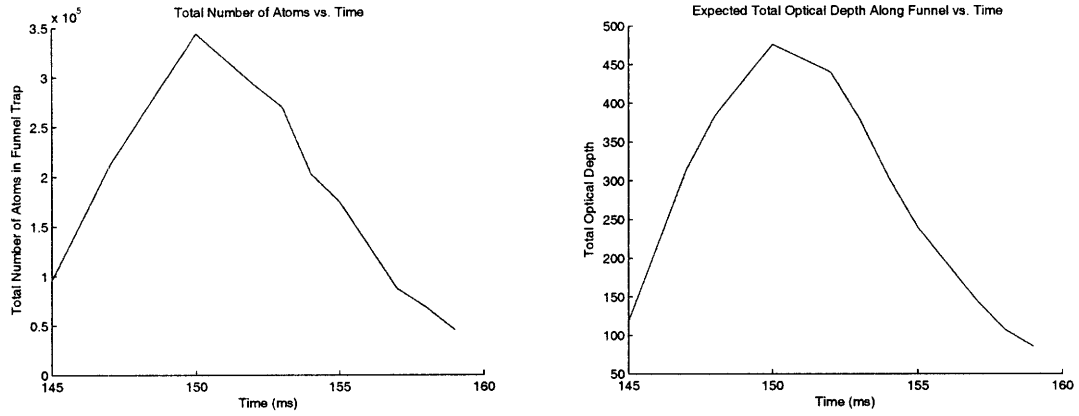

Figure 6-5: Total atom number and optical depth vs. time
The time is with respect to some t=0 in the timing sequence used to take the pictures.

6.4 Atoms in the Dipole Trap

We have just recently observed evidence of atoms being loaded into the optical dipole trap and the fiber. A clear indicator of this is the AC Stark shift of the atoms, as mentioned in section 3.4. The transition frequency is shifted down for a red-detuned trap by an amount proportional to the intensity of the laser. As the atoms become trapped in the fiber, the light intensity increases dramatically and we should see a shifted absorption peak, along with a non-shifted peak due to free atoms outside the trap. This is indeed what what we see in Fig. 6-6.

There are several features of Fig. 6-6 that are not quite clear to us at this point. First, the absorption due to atoms in the dipole trap is broadened due to the different intensities of light seen by the atoms in different parts of the dipole trap. The largest shifts should be due to atoms in the deepest part of the trap. Interestingly, the absorption curve for the trapped atoms seems to have two peaks, which are most clearly seen at 1ms and 6ms. At 2ms, the broadening is reduced, but it seems like we have lost absorption due to atoms in the deepest central part of the trap. One could speculate that this is due to some sort of motion of the atoms in the trap. Of course, the behavior of this broadening will affect our ability to address the atoms at the correct transition frequency. Therefore, we still need to have a better understanding

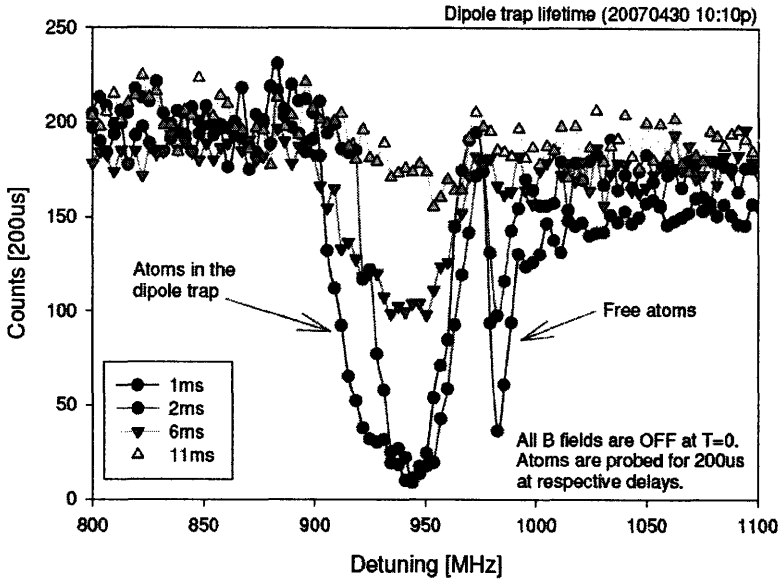

Figure 6-6: Absorption Curve of Atoms in Dipole Trap
Taken with a photon counter using the D_2 probe laser.

of the mechanisms that give rise to the features in the absorption profile.

6.5 Conclusions and Future Work

Currently, we are quite confident in our procedure for collecting atoms in the MOT and using magnetic traps to transfer them toward the fiber. We also know that there are atoms in the dipole trap. Though we currently have no direct way of measuring if they are in the fiber or somehow trapped just outside, there aren't really any mechanisms that would prevent the atoms from entering the fiber once they are in the trap.

As mentioned above, we are trying to come up with explanations for what we see from the dipole trap absorption curve and possible ways of dealing with the shifting and broadening of the transition line. One possibility is to eliminate the AC Stark shift altogether when we want to probe the atoms. This can be done by modulating

the trap at a frequency faster than that of the motion of atoms inside the trap. If the modulation frequency is high enough, the atoms should see a time-averaged trapping potential and remain confined inside the fiber. However, at the times when the trap intensity is low, the energy levels of the atoms will not be shifted. We can then probe the atoms during those times when they all have the same known transition frequencies.

There are also many ways we could optimize the current procedure once we have a more complete idea of how to load and probe the atoms in the fiber. We are currently not applying any DC biasing fields on the atoms, and doing so would eliminate ambient fields and increase the number of atoms in the MOT and magnetic traps. Various parts of the timing sequence, such as the ramping of the y direction bias field, can also be tweaked. The easiest way to do this would probably be to optimize the parameters by directly looking at the signal from atoms inside the fiber.

In the end, of course, we hope to apply this setup in the study of phenomena such as EIT and use it to implement a quantum device. Once we have determined the best way to prepare the system, we can consider what sorts of studies are possible based on the number of atoms inside the fiber and their behavior. There is constant progress being made toward reaching this next stage of the experiment, and we look forward to finding out what interesting and useful properties this novel system of trapped atoms in an optical fiber has to offer.

Appendix A

Schematics and Board Layouts for Current Controllers

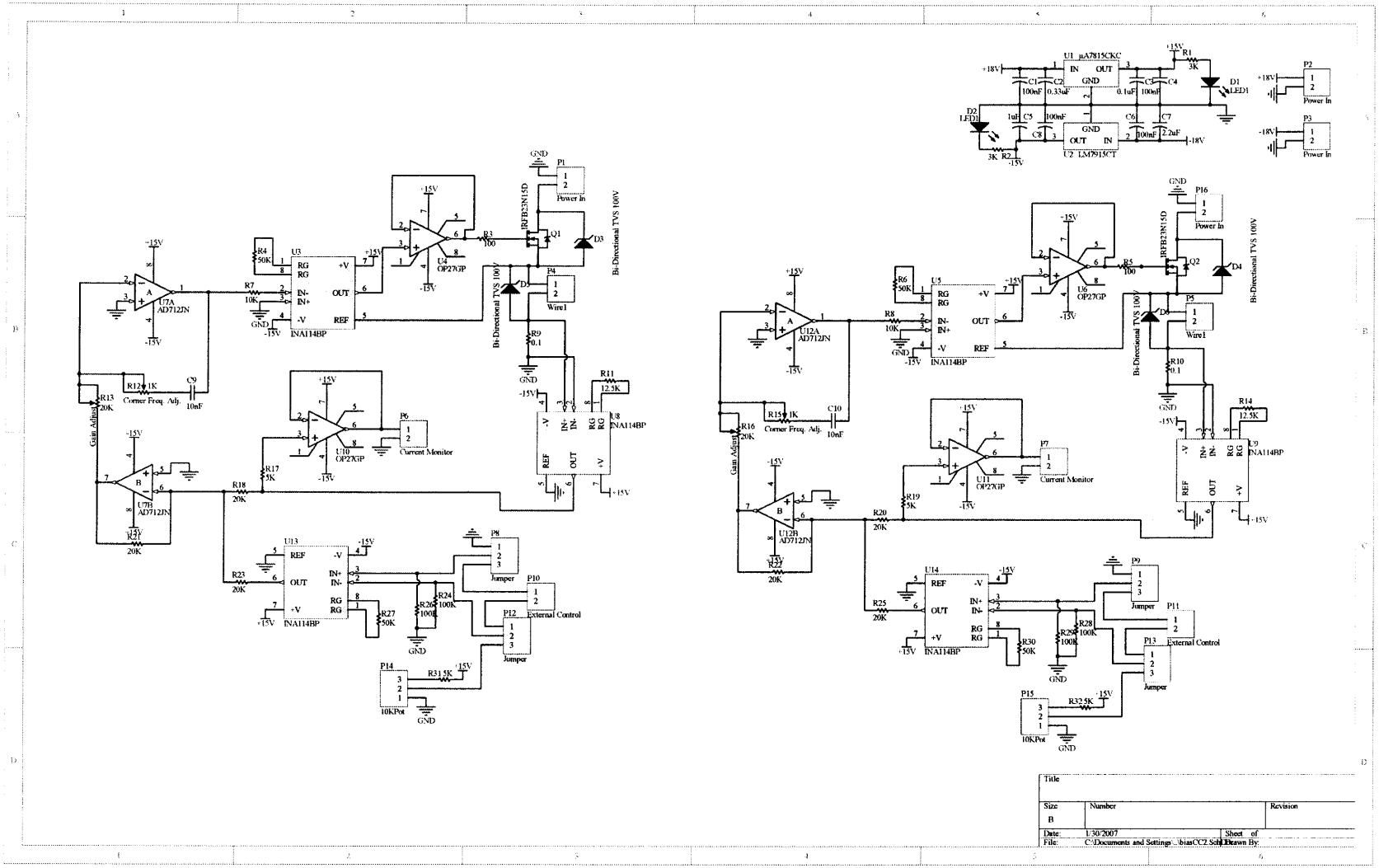

Figure A-1: Schematic for a pair of bias coil controllers.
In this and the next two schematics, the gain resistors on the INA114/111 instrumentation amplifiers may be changed depending on the range of input and output needed.

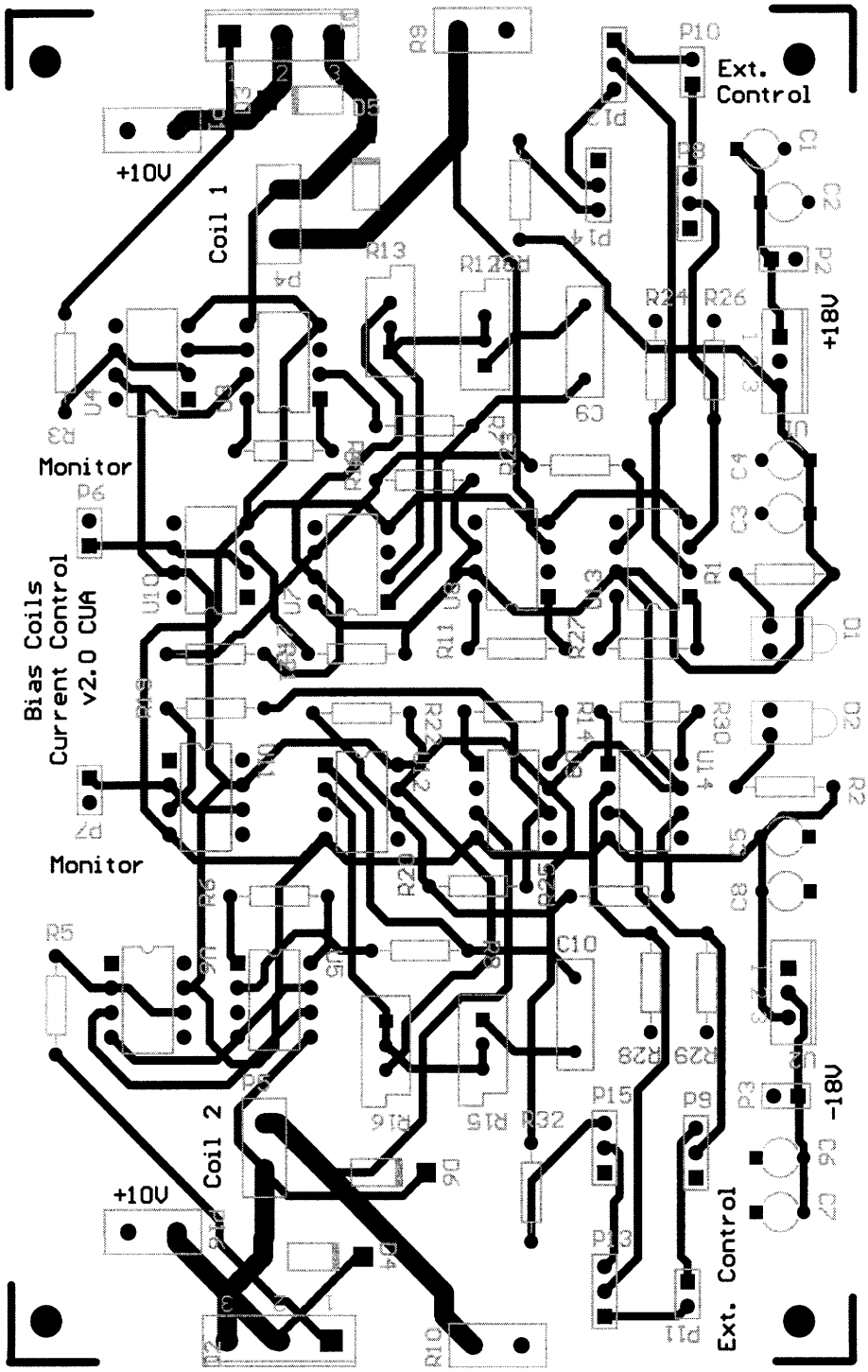

Figure A-2: Printed circuit board layout for a pair of bias coil controllers.

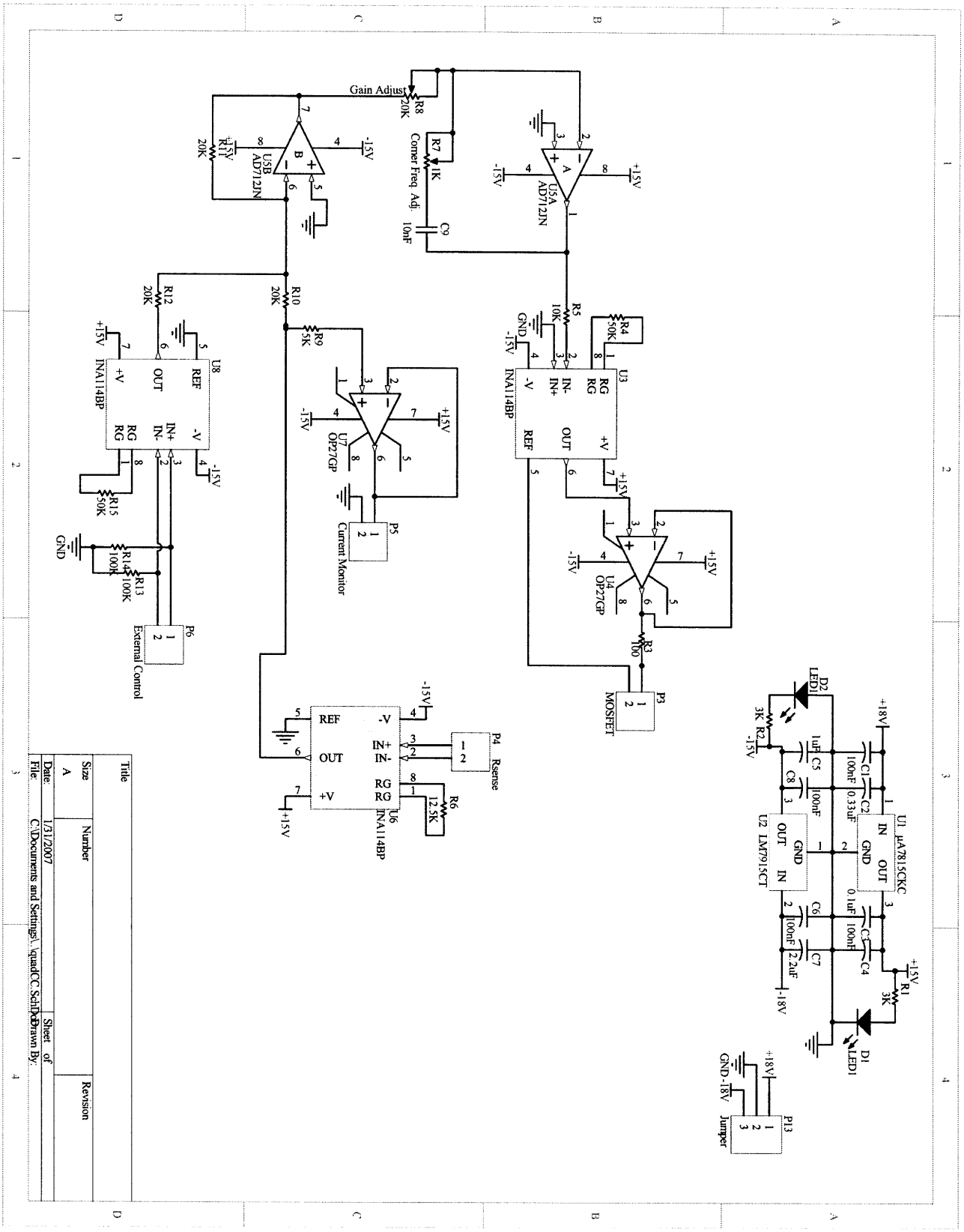

Figure A-3: Schematic for quadrupole wires current controller.

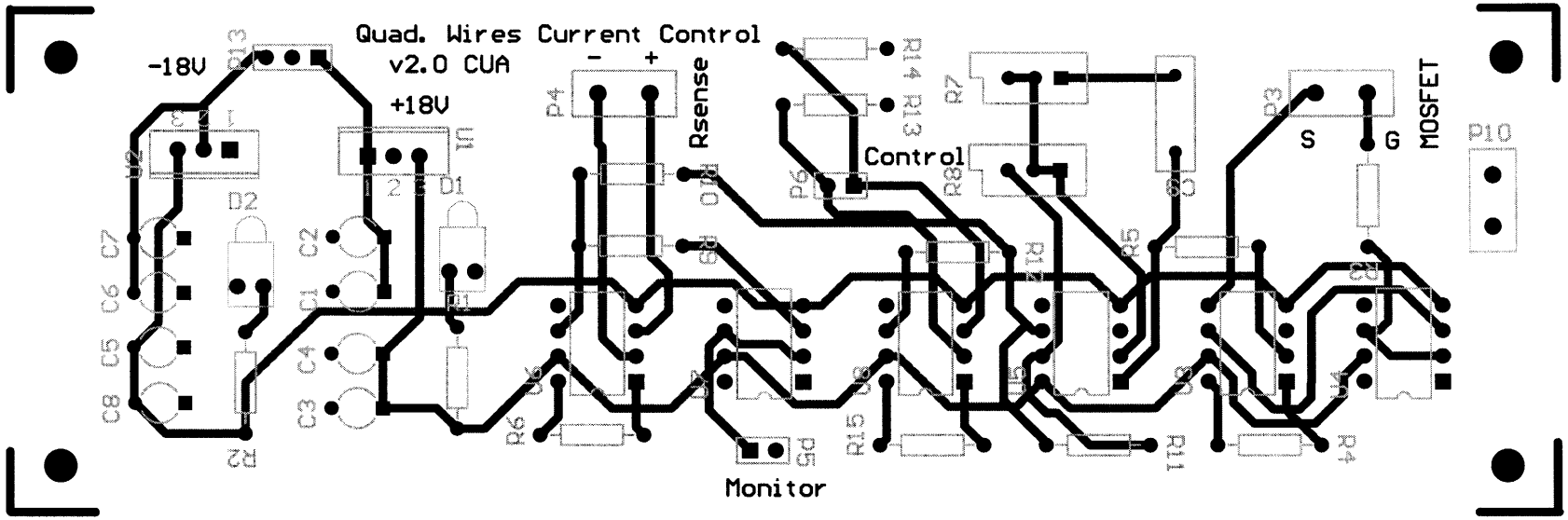

Figure A-4: Printed circuit board layout for quadrupole wires current controller.

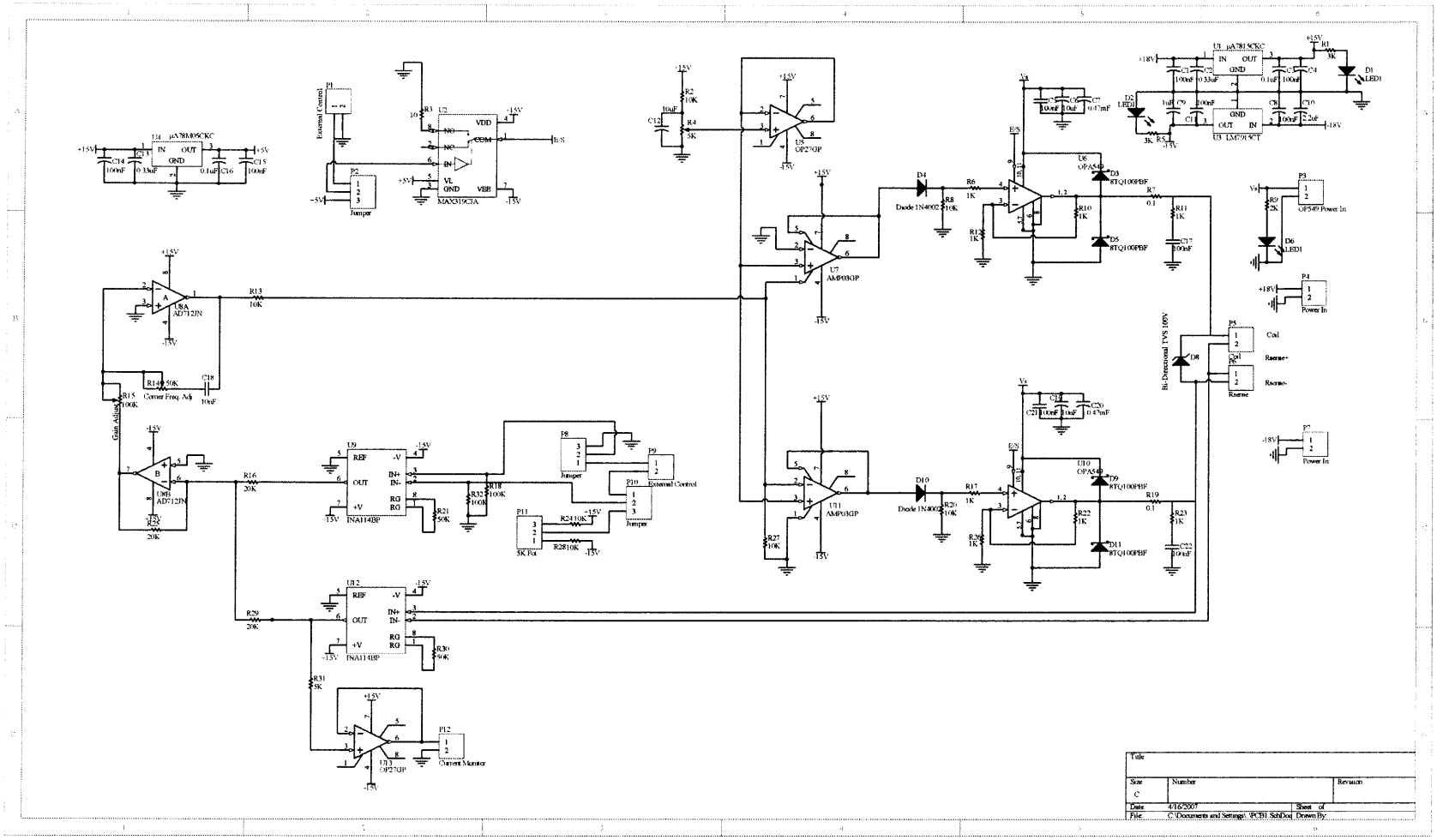

Figure A-5: Schematic for the MOT and shift coil current controller.

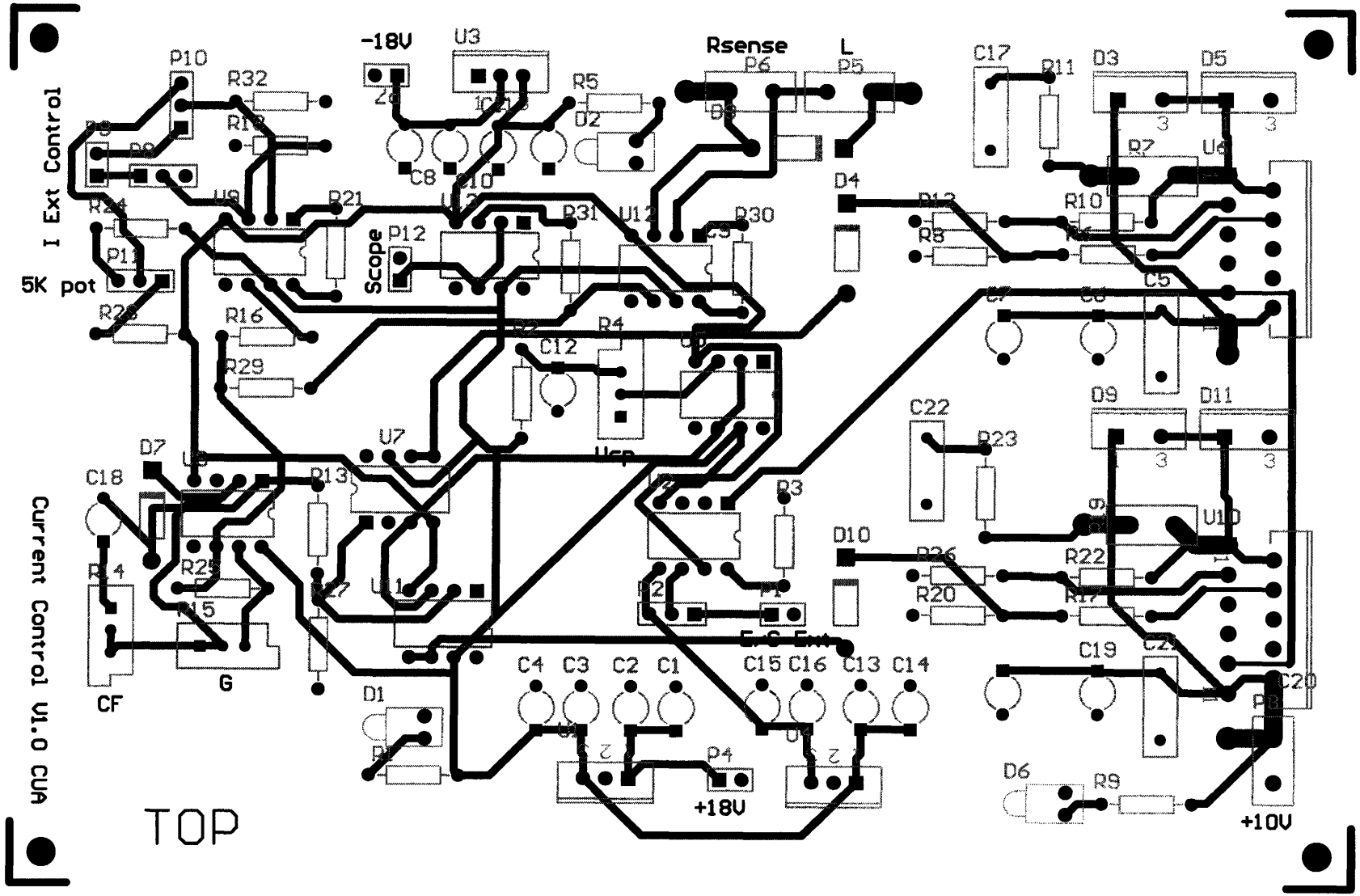

Figure A-6: Printed circuit board layout for the MOT or shift coil current controller.

Bibliography

[1] A. André *et al.*, "Nonlinear Optics with Stationary Pulses of Light," Phys. Rev. Lett. **94**, 063902 (2005).

[2] R. F. Cregan, B. J. Mangan, J. C. Knight, T. A. Birks, P. St.J. Russell, P. J. Roberts and D. C. Allan, "Single mode photonic band gap guidance of light in air," Science **285**, 1537-1539 (1999).

[3] S. Johnson, *Mathematical Methods in Nanophotonics*, course notes for 18.369, Massachuesetts Institute of Techonology (2007).

[4] S. Ghosh, J. E. Sharping, D. G. Ouzounov, and A. L. Gaeta, "Resonant Optical Interactions with Molecules Confined in Photonic Band-Gap Fibers," Phys. Rev. Lett. **94**, 093902 (2005).

[5] E. L. Raab, M. Prentiss, A. Cable, S. Chu, and D. E. Pritchard, "Trapping of Neutral Sodium Atoms with Radiation Pressure," Phys. Rev. Lett. **59**, 2631-4 (1987).

[6] C. Wieman, G. Flowers, and S. Gilbert, "Inexpensive laser cooling and trapping experiment for undergraduate laboratories," Amer. J. Phys. **63**, 317-30 (1995).

[7] D. A. Braje *Low-Light-Level Nonlinear Optics Using Electromagnetically Induced Transparency*, Ph.D. thesis, Stanford University (2004).

[8] H. Metcalf and P. van der Straten. *Laser Cooling and Trapping* (Springer, New York, 1999).

[9] S. Chu, L. Hollberg, J. E. Bjorkholm, A. Cable, and A. Ashkin, "Three dimensional viscous confinement and cooling of atoms by resonance radiation pressure," Phys. Rev. Lett. **55**, 48-51 (1985).

[10] D. Wineland and W. Itano, "Laser cooling of atoms," Phys. Rev. A **20**,1521 (1979).

[11] J. Dalibard and C. Cohen-Tannoudji, "Laser cooling below the Doppler limit by polarization gradients: simple theoretical models," J. Opt. Soc. Am. B **6**, 2023-45 (1989).

[12] A.L. Migdall, J.V. Prodan, W.D. Phillips, T.H. Bergemann, and H.J. Metcalf, "First oberservation of magnetically trapped neutral atoms," Phys. Rev. Lett. **54**, 2596 (1985).

[13] D. J. Griffiths. *Introduction to quantum mechanics.* (Prentice-Hall, Inc., 1994).

[14] R. Grimm, M. Weidemuller, and Yu. B. Ovchinnikov, "Optical dipole traps for neutral atoms," Adv. At. Mol. Opt. Phys. **42**, 95170 (2000)

[15] T. Petelski, M. Fattori, G. Lamporesi, J. Stuhler, and G.M.. Tino, Eur. Phys. J. D **22**, 279 (2003)

[16] S. Sewell, *Advanced Experimental Physics*, laboratory guide, Massachusetts Institute of Technology (2005).

[17] D. Brown, *Trapping Cold Rubidium in a Fiber*, Senior thesis, Massachusetts Institute of Technology (2007).

[18] T. Bergeman, G, Erez, and H.J. Metcalf. "Magnetostatic trapping fields for neutral atoms," Phys. Rev. A, **35**, 1535-1546 (1987).

[19] M.Abramowitz and I.A Stegun. *Handbook of Mathematical Functions with Formulas, Graphs, and Mathematical Tables.* U.S. Department of Commerce, pp. 590. Online version at: http://www.math.sfu.ca/~cbm/aands/

[20] M. Misakian, "Equations for the magnetic field produced by one or more rectangular loops of wire in the same plane," J. Res. Natl. Inst. Stand. Technol. **105**, 557 (2000).

[21] A. Oppenheim and A. Willsky, *Signals and Systems* (Prentice Hall, Upper Saddle River, 1996).

[22] T. Meyrath *Experiments with Bose-Einstein Condensation in an Optical Box*, Ph.D. thesis, The University of Texas at Austin (2005).

[23] I. Yavin, M. Weel, A. Andreyuk, and A Kumarakrishnan, "A calculation of the time-of-flight distribution of trapped atom," Am. J. Phys. **70**, 2 (2002).